

NewPINNs: Physics-Informing Neural Networks Using Conventional Solvers for Partial Differential Equations

Maedeh Makki*

Department of Mechanical Engineering, University of California Riverside

mmakk004@ucr.edu

Satish Chandran*

Department of Mathematics, University of California Riverside

schan360@ucr.edu

Maziar Raissi

Department of Mathematics, University of California Riverside

maziarr@ucr.edu

Adrien Grenier

German Innovation Center, Procter & Gamble Service GmbH

grenier.a.2@pg.com

Behzad Mohebbi

German Innovation Center, Procter & Gamble Service GmbH

mohebbi.b@pg.com

Abstract

We introduce NewPINNs, a physics-informing learning framework that couples neural networks with conventional numerical solvers for solving differential equations. Rather than enforcing governing equations and boundary conditions through residual-based loss terms, NewPINNs integrates the solver directly into the training loop and defines learning objectives through solver-consistency. The neural network produces candidate solution states that are advanced by the numerical solver, and training minimizes the discrepancy between the network prediction and the solver-evolved state. This pull-push interaction enables the network to learn physically admissible solutions through repeated exposure to the solver’s action, without requiring problem-specific loss engineering or explicit evaluation of differential equation residuals. By delegating the enforcement of physics, boundary conditions, and numerical stability to established numerical solvers, NewPINNs mitigates several well-known failure modes of standard physics-informed neural networks, including optimization pathologies, sensitivity to loss weighting, and poor performance in stiff or nonlinear regimes. We demonstrate the effectiveness of the proposed approach across multiple forward and inverse problems involving finite volume, finite element, and spectral solvers.

1 Introduction

Solving partial differential equations (PDEs) is a fundamental task in many different scientific and engineering disciplines such as electrodynamics, fluid dynamics, and solid mechanics (Jackson, 2003; Panton, 2013; Dym & Shames, 2013; Zheng, 2023). However, outside of simplified toy-models, it is nearly impossible to write down an analytical solution to a given differential equation system (Evans, 2010). As a result, myriad numerical methods such as the finite difference method (FDM), finite volume methods (FVM), finite element methods (FEM), lattice Boltzmann methods (LBM), material point methods (MPM), etc., have been developed over the centuries to solve PDEs accurately for many scientific and engineering problems (Susanne C. Brenner, 2008; LeVeque, 2007b; 2002; Stig Larsson, 2003; Mats G. Larson, 2013; Hosseini et al., 2023; Ginzburg, 2008; Ataei & Salehipour, 2024; de Vaucorbeil et al., 2020; Nguyen et al., 2023; Haughey, 2009).

*Denotes equal contribution

Over the past decade deep-learning has been used to solve many scientific and engineering problems involving differential equations. Traditional data-driven neural networks often struggle with physical consistency when modeling complex systems, requiring a prohibitively large number of samples and often failing to generalize beyond training distributions (Raissi et al., 2020). To address this, the physics-informed neural networks (PINNs) were developed as a flexible method to solve forward and inverse problems (Raissi et al., 2019; Zhao et al., 2024; Gao et al., 2022; Yang et al., 2025). In the PINNs framework, a neural network learns the solution of a PDE by having its loss function be composed of residuals of the differential equation and the boundary/initial conditions (Raissi et al., 2019). Despite their success, PINNs face significant structural limitations that hinder their reliability in complex scenarios:

- **Optimization Difficulties:** The standard PINN loss function is a complex weighted sum of PDE residuals, boundary conditions, and initial conditions. This creates a highly non-convex loss landscape that is difficult to optimize, often leading to convergence failures in stiff systems or multi-scale problems (Rathore et al., 2024; Song et al., 2024).
- **Hyperparameter Sensitivity:** Balancing the competing terms in the loss function requires tuning multiple scalar weights, a process that is often stiff and problem-dependent.
- **Spectral Bias:** Neural networks tend to learn low-frequency functions first, which causes standard PINNs to struggle with high-frequency or chaotic dynamics where the PDE residual does not provide a strong enough gradient signal for fine-scale features (Ye et al., 2024; Mustajab et al., 2024; Jin et al., 2024).

To address these challenges, many different approaches have been developed. These methods can broadly be classified into 3 distinct categories, namely PINNs, hybrid neural-numerical methods, and data-driven methods.

Physics-Informed Neural Networks (PINNs): Since the introduction of “classical” PINNs, there have been many modified versions of them to improve their performance across multiple scientific and engineering tasks (Raissi et al., 2019; Wang et al., 2024a; Jagtap et al., 2020; Lee, 2024). Wang et al. divided their simulation domain into subdomains and trained local PINNs on each one to mitigate very small and very large gradients, and also address poor scaling of PDE residuals (Wang et al., 2021).

Hybrid Neural-Numerical Models: Combining traditional numerical solvers with neural networks to use the strength of both approaches, has gained significant interest in recent years (Zhang et al., 2024; Oommen et al., 2024; Merlet, 2024). The neural ODE model implements the neural network output as a derivative in an ODE solver, and then used an integrator to solve the ODE and compute the gradients to train the network (Chen et al., 2018). The NNfoil framework that PINNs with a finite element mesh transformation to simulate subsonic, inviscid flow around airfoils (Cao & Song, 2024). Time-Stepping-Oriented Neural Network (TSOON) resolves the ill-conditioning in PINNs by adjusting the Jacobian condition number to enhance performance (Cao & Zhang, 2025). Universal Differential Equations (UDEs) splits the solution space into a multiple neural networks and feeds them into traditional solvers to train them (Rackauckas et al., 2020). The neural-initialized Newton (NiN) strategy accelerates nonlinear finite element solvers by using a pretrained physics-informed neural operator as an initial guess for Newton–Raphson iterations (Taghikhani et al., 2025). The Pretrained Finite Element Method (PFEM) introduces a two-stage hybrid framework in which a transformer-based physics-informed neural operator is trained solely from PDE constraints on unstructured point clouds and subsequently used to warm-start classical finite element solvers (Wang et al., 2026).

Data-Driven Discovery of Differential Equations: Extracting physical properties from known or measured data (i.e. inverse problems) is another critical problem in many scientific and engineering domains (Egan et al., 2024; Pu & Chen, 2023; Meidani & Barati Farimani, 2021; Xu et al., 2023). The Sparse Identification of Nonlinear Dynamics (SINDy) algorithm is a popular method for discovering governing equations from data by expressing derivatives as sparse combinations of candidate (often polynomial) basis

functions of a few dominant terms, and uses sparse regression to identify them from time series data (Huang et al., 2022). However SINDy requires a comprehensive library of functions and often fail to handle noisy data (Brunton et al., 2016). Raissi et al. used a PINN-like training approach to find the unknown parameters of equations by approximating the solution and non-linear differential operators as neural networks and fitting the residual to the observed data (Raissi, 2018). Long et al. developed PDE-Net 2.0, which learns coefficients of PDEs from time dependent data by combining both convolutional and symbolic neural networks (Long et al., 2019). Neural operator methods such as DeepONet and Fourier Neural Operators have also gained traction in recent years. The neural operator frameworks aim to learn global mappings between function spaces, typically by training on large datasets of input–output pairs generated by numerical solvers (Lu et al., 2021; Li et al., 2020). While these approaches have demonstrated strong performance in data-rich regimes, they rely on extensive precomputed datasets and primarily function as supervised surrogate models.

To address these fundamental challenges, we introduce NewPINNs, a novel framework that fundamentally alters how physics is injected into the network. Instead of forcing the network to minimize a PDE residual derived via automatic differentiation, NewPINNs couples the network with a traditional numerical solver in a “pull-push” closed-loop solver-consistency training procedure (see Figure 1).

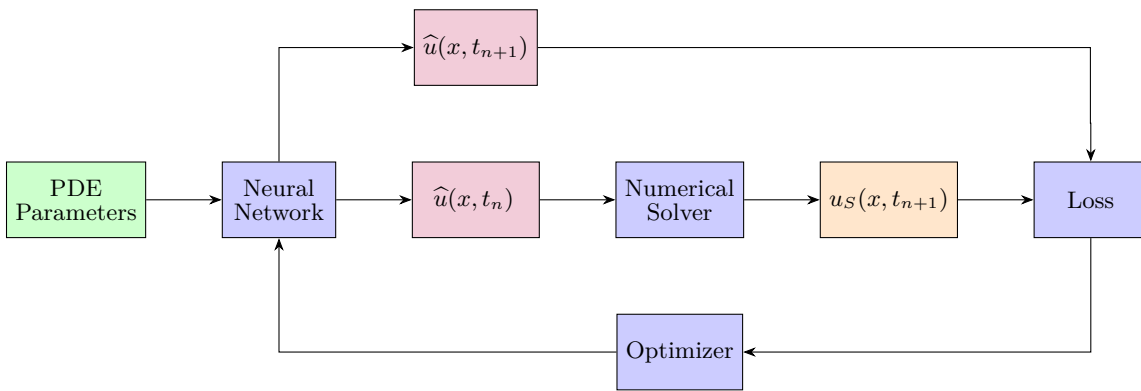


Figure 1: Transient NewPINNs: At each training iteration, the neural network produces a candidate solution at time t_n which is advanced to t_{n+1} by the numerical solver. A solver-consistency loss compares this solver-evolved state with the network’s prediction at the next time step, enforcing temporal consistency under solver evolution. The solver is treated as a black-box operator and does not participate in gradient computation.

In this framework, the neural network acts as a generator of candidate solution states (“pull”), while the external solver defines a numerical evolution operator that advances these states according to a prescribed discretization (“push”). The loss function is then defined as a solver-consistency objective, which enforces agreement between the network’s prediction and the result of applying the solver to that prediction. This approach offers several distinct advantages over standard PINNs:

- **Simplified Optimization:** By removing PDE residuals and boundary constraints from the loss function, we eliminate the conflict between competing loss terms and the need for delicate hyperparameter tuning.
- **Solver Agnosticism:** Unlike “differentiable physics” approaches that require specialized differentiable solvers, NewPINNs treats the solver as a black box. This allows the use of established, highly optimized commercial solvers (e.g., COMSOL, Ansys) and does not require the solver to be differentiable.
- **Surrogate Modeling:** By enforcing consistency under solver evolution, the network is trained to produce physically admissible states that respect the stability and invariance properties of the underlying numerical discretization. Thus the neural network effectively learns to become a fast surrogate (or “twin”) of the solver, capable of predicting complex, non-linear, and even chaotic dynamics that standard PINNs can often fail to capture.

Viewed from an operator perspective, NewPINNs does not attempt to learn a global mapping from inputs to solutions using fixed solver-generated datasets. Instead, it enforces physical consistency by minimizing a solver-induced operator residual evaluated on the network’s own predictions. The solver does not act as a teacher or data generator, but rather as a constraint operator whose action defines admissible solutions through invariance or consistent temporal evolution (see Section 2.3). This distinction allows NewPINNs to operate effectively in data-scarce regimes and to leverage legacy numerical solvers as black-box components, while maintaining a principled notion of physical validity without the need for explicit PDE residual losses.

The source code is available on <https://github.com/chandran-satish/NewPINNs>.

2 Methodology

In general, we are interested in solving partial differential equations (PDEs) of the form

$$\begin{aligned} \frac{\partial u}{\partial t} &= \mathcal{N}[u(x, t); \alpha] \quad \forall (x, t) \in \Omega \times [0, T] \\ \mathcal{I}[u(x, 0)] &= 0 \quad \forall x \in \Omega \\ \mathcal{B}[u(x, t)] &= 0 \quad \forall (x, t) \in \partial\Omega \times [0, T] \end{aligned} \tag{1}$$

where \mathcal{N} is a non-linear differential operator parameterized by α , Ω is the spatial domain in \mathbb{R}^d and $\partial\Omega$ the corresponding boundary, \mathcal{B} and \mathcal{I} denote the sets of boundary and initial conditions respectively, and u is the unknown solution function.

2.1 Physics-Informed Neural Networks (PINNs)

Physics-Informed Neural Networks (PINNs) aim to approximate u using neural networks by incorporating the PDE directly into the loss function. During training, the network is evaluated at a set of collocation points in the spatio-temporal domain, and automatic differentiation is used to compute the residuals of the PDE and auxiliary constraints. These residuals form the basis of the loss function that drives the optimization of θ .

The standard PINN loss function is composed of multiple terms, corresponding to the PDE constraint, boundary condition (BC) constraint, or initial condition (IC) constraint

$$\mathcal{L}(\theta) = \lambda_{PDE}\mathcal{L}_{PDE} + \lambda_{BC}\mathcal{L}_{BC} + \lambda_{IC}\mathcal{L}_{IC}, \tag{2}$$

where each term measures the mean squared residual at (randomly sampled) collocation points which are given by

$$\mathcal{L}_{PDE} = \frac{1}{N_{PDE}} \sum_{i=1}^{N_{PDE}} \left\| \frac{\partial}{\partial t} \hat{u}(x_i, t_i; \theta) - \mathcal{N}[\hat{u}(x_i, t_i; \theta)] \right\|^2 \text{ with } x_i \in \Omega, \tag{3}$$

$$\mathcal{L}_{BC} = \frac{1}{N_{BC}} \sum_{j=1}^{N_{BC}} \left\| \mathcal{B}[\hat{u}(x_j, t_j; \theta)] \right\|^2 \text{ with } x_j \in \partial\Omega, \tag{4}$$

and

$$\mathcal{L}_{IC} = \frac{1}{N_{IC}} \sum_{k=1}^{N_{IC}} \left\| \mathcal{I}[\hat{u}(x_k, t_0; \theta)] \right\|^2 \text{ with } x_k \in \Omega, \tag{5}$$

where N_{PDE} , N_{BC} , and N_{IC} refer to the total number of collocation points sampled from the domain for each residual term respectively. The weights λ_{PDE} , λ_{BC} , and λ_{IC} allow for the tuning the relative importance of each term in the loss function. This formulation enables PINNs to unify data-driven learning and physics-based modeling. However it also introduces challenges, such as sensitivity to the choice of weights, difficulty in training for stiff PDEs, and potential imbalance between residual components, especially in multi-scale or convection-dominated flows (Ji et al., 2021).

2.2 NewPINNs: Physics-Informing Neural Networks using Numerical Solvers

The NewPINNs approach differs from the PINNs framework in that it directly uses traditional numerical solvers to guide the training of the neural network. Generally, numerical solvers work by discretizing the spatial and temporal domains and compute the approximate solution at every discrete time step (Blazek, 2015; LeVeque, 2007a). Solution over the entire domain is obtained by forward step-by-step iterations starting from the initial time t_0 and initial conditions. In mathematical terms, we say a solver \mathcal{S} takes in an initial state $u(x, t_0)$, along with boundary conditions $\mathcal{B}[u]$ and a set of physical parameters α , and pushes it forward to time t_{N_s} in discrete time steps i.e.,

$$u(x, t_{N_s}) = \mathcal{S}[u(x, t_0), \mathcal{B}[u], \alpha, N_s]. \quad (6)$$

Here, N_s is the number of required iterations inside the solver to compute $u(x, t_{N_s})$ from $u(x, t_0)$. For many PDEs, we can also view this solver mapping as an approximation of the semi-group operator of the system (Chen & Wu, 2023; Tsai, 2018.). One important note here is that the spatial domain can be discretized in a variety of ways depending on the numerical solver of choice. For example finite-difference solvers will discretize the spatial domain into discrete grid points, while finite element solvers will discretize the spatial domain as a mesh which can take on many complex geometries (Bathe, 2006). Thus going forward, we omit the discrete indices of the spatial domain for readability.

2.2.1 Forward Problems

In forward problems, we are interested in finding the solution function u , given the PDE, the initial and boundary conditions, and the parameters of the equation (i.e., α).

NewPINNs for Transient Systems: Most traditional numerical solvers for time-dependent PDEs (e.g., finite difference methods, finite element methods, or finite volume methods) do not explicitly incorporate continuous time t in their formulations. Instead, they work with discrete time steps Δt and a total number of time steps N_t , and iteratively advance the solution from one step to the next (Gustafsson et al., 2013). In this regard, and according to the Equation (6), traditional solvers can accept a value as initial condition—meaning the neural network f_{NN} can provide its output to the solver (pull mechanism). The solver then applies the boundary conditions $\mathcal{B}[u]$, and physical properties α to compute the next step solution by taking the given N_s iterations, and returns its computed value to the neural network (push mechanism) i.e.

$$u(x, t_{N_s}) = \mathcal{S}[f_{NN}(t_0), \mathcal{B}[u], \alpha, N_s]. \quad (7)$$

The main idea for transient NewPINNs is to treat each temporal grid point as a virtual initial time, and feed the physical parameters of our system and the temporal grid point into our neural network which outputs the approximate PDE solution along the spatial domain i.e.

$$\hat{u}(x, t_n; \theta) = f_{NN}(t_n, \alpha; \theta). \quad (8)$$

Then, the numerical solver is applied to each $\hat{u}(x, t_n; \theta)$ to push it forward in time by one temporal step to obtain $u(x, t_{n+1})$ i.e.

$$u_{\text{solver}}(x, t_{n+1}) = \mathcal{S}[\hat{u}(x, t_n; \theta), \mathcal{B}[u], \alpha, N_s]. \quad (9)$$

Here, we use the index n to denote the temporal sequence. In a real experiment, it takes N_s steps for the solver to compute the output from the network prediction. The solver output is then compared with the neural network output. This results in the loss function

$$\mathcal{L}_{\text{solver}}(\theta) = \frac{1}{N_\alpha} \sum_{\alpha} \sum_{n=0}^{N_t-1} \left\| f_{NN}(t_{n+1}, \alpha; \theta) - \mathcal{S}[\hat{u}(x, t_n; \theta), \mathcal{B}[u], \alpha, N_s] \right\|_{L^2(\Omega)}^2. \quad (10)$$

Here $\|\cdot\|_{L^2(\Omega)}$ refers to the (discrete) L^2 norm over the spatial domain Ω . Another important aspect of transient systems is that they are not invariant to initial states unlike steady-state systems, i.e. different initial conditions $\mathcal{I}[u(x, t_0)]$ in Equation (1) will result in different spatiotemporal trajectories for the system.

As a result, it is also critical to enforce the initial conditions of the system for the neural network predictions. This is achieved by adding the corresponding loss term

$$\mathcal{L}_{\text{IC}}(\theta) = \frac{1}{N_\alpha} \sum_{\alpha} \left\| \mathcal{I}[f_{\text{NN}}(t_0, \alpha)] \right\|_{L^2(\Omega)}^2. \quad (11)$$

This results in the total loss function being

$$\mathcal{L}_{\text{transient}}(\theta) = \mathcal{L}_{\text{IC}}(\theta) + \mathcal{L}_{\text{solver}}(\theta). \quad (12)$$

The combination of these loss functions ensure strict adherence to the specified initial conditions, and that the network's solution remains consistent with the solver's output for the spatio-temporal trajectories. Minimizing the proposed $\mathcal{L}_{\text{transient}}(\theta)$ results in a neural network which can output the PDE solution along the specified spatiotemporal grid points. The pseudo-code for training the neural network for transient systems is given in Algorithm (1). We consider neural architectures that either (i) output a discretized field over Ω directly (e.g. U-Nets), written as $f_{\text{NN}}(t, \alpha; \theta)$, or (ii) output pointwise solution values for given spatiotemporal coordinates (x, t) , written as $f_{\text{NN}}(x, t, \alpha; \theta)$, which are then evaluated over a spatial grid to form a state vector. For notational simplicity, we refer to both cases using the unified notation $f_{\text{NN}}(t, \alpha; \theta)$.

Algorithm 1: Training Routine for Transient NewPINNs

Input : Training set of physical parameters α_{train} , boundary conditions $\mathcal{B}[u]$, initial conditions $\mathcal{I}[u(x, t_0)]$, number of training epochs M , learning rate η
Output: Trained network parameters θ

```

1 function TransientNewPINNs( $N_s, \alpha_{\text{train}}, \mathcal{B}[u], M$ )
2   for  $n \leftarrow 0$  to  $M - 1$  do
3      $\mathcal{L}(\theta) \leftarrow 0$ 
4     for  $\alpha \in \alpha_{\text{train}}$  do
5        $\mathcal{L}_{\text{IC}} \leftarrow \|\mathcal{I}[f_{\text{NN}}(t_0, \alpha)]\|^2$  // Initial Condition Loss
6        $\mathcal{L}(\theta) \leftarrow \mathcal{L}(\theta) + \mathcal{L}_{\text{IC}}$ 
7       for  $k \leftarrow 0$  to  $N_t - 1$  do
8          $\hat{u}(x, t_k, \alpha; \theta) \leftarrow f_{\text{NN}}(t_k, \alpha; \theta)$  // Network predicts current state
9          $u_{\text{solver}}(x, t_{k+1}, \alpha) \leftarrow \mathcal{S}[\hat{u}, \alpha, \mathcal{B}[u]]$  // Solver pushes to next state
10         $\mathcal{L}(\theta) \leftarrow \mathcal{L}(\theta) + \|f_{\text{NN}}(t_{k+1}, \alpha; \theta) - u_{\text{solver}}(x, t_{k+1}, \alpha)\|^2$ 
11     $\theta \leftarrow \theta - \eta \nabla_{\theta} \mathcal{L}$ 

```

NewPINNs for Steady-State Systems: For many physical systems, it is known that the PDE will converge to an equilibrium (i.e. steady-state) solution $u_{\text{eq}}(x)$ as t approaches infinity (Boussaid et al., 2015; LeVeque, 2007a). In the numerical setting, this means there is some sufficiently large number of solver iterations N_∞ that will ensure this, i.e.

$$u_{\text{eq}}(x) = \mathcal{S}[u(x, t_0), \mathcal{B}[u], \alpha, N_\infty]. \quad (13)$$

Of course, if the equilibrium solution is fed into the solver then it will return the equilibrium solution again i.e.

$$u_{\text{eq}}(x) = \mathcal{S}[u_{\text{eq}}(x), \mathcal{B}[u], \alpha, N], \quad \forall N > 0, \quad (14)$$

for any number of iterations N (Marwah et al., 2023; Granas & Dugundji, 2003). The key idea behind the NewPINNs framework for steady state systems is that we can exploit this fixed/equilibrium point to help train the neural network. We want to train a neural network $f_{\text{NN}}(\alpha; \theta)$ that takes in the physical parameters α as an input and outputs $u_{\text{eq}}(x)$ directly. To derive the NewPINNs loss function, we can take the output of the neural network, and then feed it as an input to the solver and run the solver for a small number of iterations $N_s \ll N_\infty$. If the neural network is accurate, the mean-squared error should be close to zero. In mathematical terms, we define the NewPINNs loss function as

$$\mathcal{L}(\theta) = \frac{1}{N_\alpha} \sum_{\alpha} \left\| f_{\text{NN}}(\alpha; \theta) - \mathcal{S}[f_{\text{NN}}(\alpha; \theta), \mathcal{B}[u], \alpha, N_s] \right\|_{L^2(\Omega)}^2 \quad (15)$$

where α is the set of physical parameters we are interested in training over and N_α is the number of physical parameter samples. The pseudo-code for training the neural network in steady state systems is given in Algorithm (2).

Algorithm 2: Training Routine for Steady-State NewPINNs

Input : Number of solver iterations N_s , training set of physical parameters α_{train} , boundary conditions $\mathcal{B}[u]$, number of training epochs M , learning rate η

Output: Trained network parameters θ

```

1 function SteadyStateNewPINNs( $N_s, \alpha_{\text{train}}, \mathcal{B}[u], M$ )
2   for  $n \leftarrow 0$  to  $M - 1$  do
3      $\mathcal{L}(\theta) \leftarrow 0$                                      // Initialize epoch loss
4     for  $\alpha \in \alpha_{\text{train}}$  do
5        $\hat{u}(x, \alpha; \theta) \leftarrow f_{\text{NN}}(\alpha; \theta)$            // Get neural network prediction
6        $u_{\text{solver}}(x, \alpha) \leftarrow \mathcal{S}[\hat{u}, \alpha, \mathcal{B}[u], N_s]$  // Feed into numerical solver
7        $\mathcal{L}(\theta) \leftarrow \mathcal{L}(\theta) + \|\hat{u}(x, \alpha; \theta) - u_{\text{solver}}(x, \alpha)\|^2$  // Compute mean squared error
8      $\theta \leftarrow \theta - \eta \nabla_{\theta} \mathcal{L}$                          // Perform gradient descent update

```

The critical idea here is that by coupling the neural network and numerical solver in training, the neural network is trained to become a “surrogate/twin” of the numerical solver. This coupling allows the solver to “pull” the neural network into the correct physical solution space. It is also important to note here that unlike PINNs which have explicit loss terms for the boundary conditions, here the boundary conditions are directly enforced by the numerical solver itself.

2.2.2 Inverse Problems

In this section we focus on the methodology for inverse problems under the NewPINNs framework. The goal is to discover unknown physical parameter variables that satisfy Equation (1) from noisy observed data $u_{\text{ob}}(x, t)$. To achieve this, we introduce a novel training methodology that couples the forward and inverse components. The top part of this loop structure has the forward component at top as derived from the approach we discussed in section 2.2.1 to solve Equation (1) which generalizes the neural network solution over a range of physical parameters α . The bottom of the loop structure then uses the same neural network from the forward part to solve the inverse problem. The inverse component of the loop targets the recovery of defined learnable variables β by minimizing the inverse loss, given as

$$\mathcal{L}(\beta) = \frac{1}{N_t} \sum_{i=0}^{N_t-1} \left\| f_{\text{NN}}(t, \beta; \theta) - u_{\text{ob}}(x, t) \right\|_{L^2(\Omega)}^2. \quad (16)$$

The inverse component of the loop benefits from the forward component’s learning of the underlying physics. The external solver remains non-differentiable; the inverse step differentiates only through the neural surrogate $f_{\text{NN}}(\cdot; \theta)$ whose parameters have been constrained by solver-consistency training. The pseudo-code for solving inverse problems is given in Algorithm (3).

2.3 Relation to Distillation and Solver-Coupled Learning

Although NewPINNs leverages numerical solvers during training, it is fundamentally different from supervised surrogate modeling approaches in which a neural network is trained to regress directly onto solution fields generated by a solver. In supervised surrogates, the solver provides fixed labeled data, and the network minimizes a discrepancy between its output and precomputed solver trajectories. NewPINNs does not rely on such offline datasets or static targets. Instead, the numerical solver defines a physics-based consistency operator that evaluates the validity of the network’s own predictions. During training, the neural network produces a candidate solution, which is reinserted into the solver and advanced forward in time or iteration. The loss penalizes inconsistencies between the network output and the solver response to that same output. As a result, the solver does not act as a static teacher but as a dynamic, state-dependent operator whose output depends explicitly on the network prediction. This closed-loop formulation ensures that the training signal is governed by physical consistency rather than by direct imitation of solver-generated data.

Algorithm 3: Training Routine for Inverse NewPINNs

Input : Training set of physical parameters α_{train} , boundary conditions $\mathcal{B}[u]$, initial conditions $\mathcal{I}[u(x, t_0)]$, initial guess for learnable physical parameter β , number of training epochs M , learning rates η_{fw} and η_{inv} , observed data u_{ob}

Output: Trained network parameters θ , learnable parameter β

```
1 function InverseNewPINNs( $N_s, \alpha_{\text{train}}, \mathcal{B}[u], M$ )
2   for  $n \leftarrow 0$  to  $M - 1$  do
3      $\mathcal{L}(\theta) \leftarrow 0$ 
4      $\vdots$ 
5      $\theta \leftarrow \theta - \eta_{\text{fw}} \nabla_{\theta} \mathcal{L}$                                 // Execute Transient NewPINNs training loop
6      $\mathcal{L}(\beta) \leftarrow 0$ 
7     for  $k \leftarrow 1$  to  $N_t - 1$  do
8        $\hat{u}(x, t_k, \beta; \theta) \leftarrow f_{\text{NN}}(t_k, \beta; \theta)$           // Get neural network prediction
9        $\mathcal{L}(\beta) \leftarrow \mathcal{L}(\beta) + \|\hat{u}(x, t_k, \beta; \theta) - u_{\text{ob}}(x, t_k)\|^2$  // compute inverse loss
10       $\beta \leftarrow \beta - \eta_{\text{inv}} \nabla_{\beta} \mathcal{L}(\beta)$                                 // Update the learnable parameter  $\beta$ 
```

NewPINNs is also distinct from teacher–student distillation and teacher forcing strategies commonly used in machine learning. In distillation, a student network is trained to reproduce fixed outputs produced by a teacher model, and the teacher behavior is independent of the student’s predictions. In contrast, the solver output in NewPINNs depends directly on the network’s current state, and no fixed teacher labels are provided. Furthermore, unlike teacher forcing methods for sequential models, where ground-truth states are injected during training to stabilize optimization, NewPINNs preserves the closed-loop feedback between successive predictions and solver evaluations. The network is always trained on its own outputs passed through the solver. This ensures that learning enforces fixed-point consistency in steady-state systems and local semi-group consistency in transient systems. Consequently, NewPINNs differs fundamentally from both supervised distillation and sequential training heuristics, and instead learns solutions that are constrained by the underlying physics encoded in the numerical solver.

The steady-state formulation of NewPINNs is also related to deep equilibrium models and fixed-point-based learning approaches, which characterize solutions as equilibria of implicit operators (Bai et al., 2019; 2020; Winston & Kolter, 2021; Marwah et al., 2023). In NewPINNs, the numerical solver itself defines the fixed-point operator, and training minimizes the discrepancy between the network output and the solver-applied network output. Unlike deep equilibrium networks, which introduce learned implicit layers and require specialized techniques for stability and gradient computation, NewPINNs relies on the numerical solver iterations to define the equilibrium structure. This shifts the burden of stability and convergence from the neural network architecture to the numerical solver, which often have strong theoretical guarantees. Consequently, NewPINNs provides a physics-driven fixed-point formulation that preserves the interpretability and robustness of classical solvers while benefiting from the expressive power of neural networks.

2.4 Solver-Consistency Guarantees for NewPINNs

The loss formulations used in NewPINNs admit a natural interpretation in terms of *solver-consistency*: the neural network is trained to produce states that are approximately invariant under the action of a chosen numerical solver. This perspective allows us to establish precise *a posteriori* error bounds relating the magnitude of the NewPINNs residuals to the deviation from solver-consistent solutions, without requiring explicit evaluation of differential equation residuals.

Throughout this section, all norms are taken to be the discrete norms induced by the solver state space (e.g. L^2 norms on grid functions or finite element coefficient vectors), which coincide with the norms used in the training objectives.

Steady-State NewPINNs. For fixed physical parameters α and boundary conditions $B[u]$, let the numerical solver define an iteration operator

$$T_\alpha(u) := S[u, B[u], \alpha, N_s], \quad (17)$$

where N_s denotes a fixed number of internal solver iterations. A steady-state solution u_α^* satisfies the fixed-point condition

$$T_\alpha(u_\alpha^*) = u_\alpha^*. \quad (18)$$

Proposition 1 (A posteriori control via fixed-point residual). *Assume that a steady-state solution u_α^* exists and that the solver operator T_α is locally contractive in a neighborhood \mathcal{U} of u_α^* , i.e. there exists a constant $q \in (0, 1)$ such that*

$$\|T_\alpha(u) - T_\alpha(v)\| \leq q\|u - v\|, \quad \forall u, v \in \mathcal{U}. \quad (19)$$

Then for any network prediction $u = f_{\text{NN}}(\alpha; \theta) \in \mathcal{U}$, the NewPINNs steady-state residual

$$R(u) := u - T_\alpha(u) \quad (20)$$

provides an explicit bound on the distance to equilibrium:

$$\|u - u_\alpha^*\| \leq \frac{1}{1 - q} \|R(u)\|. \quad (21)$$

Proof. Since $u_\alpha^* = T_\alpha(u_\alpha^*)$, we write

$$\begin{aligned} \|u - u_\alpha^*\| &\leq \|u - T_\alpha(u)\| + \|T_\alpha(u) - T_\alpha(u_\alpha^*)\| \\ &\leq \|R(u)\| + q\|u - u_\alpha^*\|, \end{aligned} \quad (22)$$

where the final inequality follows from the contractivity of T_α . Rearranging yields the stated bound. \square

This result shows that minimizing the steady-state NewPINNs loss enforces proximity to a solver-consistent equilibrium whenever the underlying solver iteration is locally stable. Importantly, the bound is independent of the neural network architecture and relies solely on properties of the numerical solver.

Transient NewPINNs. For time-dependent problems, let the solver define a one-step evolution operator

$$T_{\alpha, \Delta t}(u^n) := S[u^n, B[u], \alpha, N_s], \quad (23)$$

which approximates advancement from time t_n to $t_{n+1} = t_n + \Delta t$. We denote by $\hat{u}^n = f_{\text{NN}}(t_n, \alpha; \theta)$ the neural network prediction at time t_n .

Proposition 2 (Solver-consistency stability for transient systems). *Assume that $T_{\alpha, \Delta t}$ is Lipschitz continuous on the relevant state set with constant $L \geq 0$, i.e.*

$$\|T_{\alpha, \Delta t}(u) - T_{\alpha, \Delta t}(v)\| \leq L\|u - v\|. \quad (24)$$

Define the one-step NewPINNs residuals by

$$\varepsilon_n := \|\hat{u}^{n+1} - T_{\alpha, \Delta t}(\hat{u}^n)\|. \quad (25)$$

Then, let $\{u^n\}$ denote the solver-consistent rollout initialized at $u^0 = \hat{u}^0$, the deviation between the neural trajectory and the solver trajectory satisfies

$$\|\hat{u}^n - u^n\| \leq \sum_{k=0}^{n-1} L^{n-1-k} \varepsilon_k. \quad (26)$$

Proof. By definition,

$$\begin{aligned}
\|\hat{u}^{n+1} - u^{n+1}\| &= \|\hat{u}^{n+1} - T_{\alpha, \Delta t}(u^n)\| \\
&\leq \|\hat{u}^{n+1} - T_{\alpha, \Delta t}(\hat{u}^n)\| + \|T_{\alpha, \Delta t}(\hat{u}^n) - T_{\alpha, \Delta t}(u^n)\| \\
&\leq \varepsilon_n + L\|\hat{u}^n - u^n\|.
\end{aligned} \tag{27}$$

Iterating this inequality yields the stated bound. \square

The solver-consistency perspective also clarifies the sensitivity of NewPINNs to neural network initialization (see Appendix A.2). The training objective enforces that network predictions lie near invariant sets or stable trajectories of the solver-induced operators, but it does not prescribe which invariant set is selected when multiple solver-consistent states exist, nor does it guarantee global attraction to the physically relevant solution. Unfavorable or biased initialization of the neural network may place early predictions outside the basin of attraction of the desired fixed point or trajectory, causing optimization to converge toward spurious solver-consistent states.

In practice, such initialization effects can have more severe consequences than merely converging to an incorrect equilibrium. When early network predictions violate implicit solver assumptions (e.g. positivity, boundedness, CFL-type stability conditions, or regularity requirements), the numerical solver may fail to advance reliably, producing undefined states such as `NaN` or `Inf`. Because the solver-consistency loss evaluates the solver's action on the network's own predictions, these numerical failures directly disrupt training and may cause divergence or premature termination, even when the underlying PDE admits a well-posed solution.

In the steady-state setting, this behavior may appear as rapid solver breakdown or non-convergence when initialized near unstable or non-physical equilibria admitted by the discrete scheme. In the transient setting, initialization-induced violations of solver stability can be amplified when the evolution operator has a Lipschitz constant $L \geq 1$, leading not only to trajectory divergence but also to catastrophic numerical failure. These outcomes are consistent with the theoretical bounds above, which provide only local control under stability assumptions and do not preclude solver breakdown outside stable regions.

This analysis highlights that NewPINNs inherits both the stability properties and the numerical failure modes of the underlying solver. Consequently, robust training may require careful initialization, solver-aware regularization, curriculum strategies, or warm-starting from coarse or classical solutions to ensure that network predictions remain within solver-admissible regions throughout training.

3 Experiments

In this section we demonstrate the NewPINNs framework for across three different solver types, namely the finite volume method, the finite element method, and a spectral method.

3.1 The 2D Fokker–Planck Equation using the Finite Volume Method

Forward problem. We demonstrate the applicability of NewPINNs to the two-dimensional Fokker–Planck equation, a prototypical convection–diffusion equation arising in statistical physics and stochastic processes as the evolution equation for probability densities under diffusion and drift in an external potential.

We consider the Fokker–Planck equation on the unit square domain $\Omega = [0, 1]^2$,

$$\frac{\partial u}{\partial t} = \nabla \cdot (\nabla u + u \nabla V), \quad (x, y) \in \Omega, \tag{28}$$

where $u(x, y, t)$ denotes a probability density and $V(x, y)$ is a parameterized potential of the form

$$V(x, y) = \alpha \sin(2\pi x) \sin(2\pi y), \quad \alpha \in [1, 2]. \tag{29}$$

For confining potentials and no-flux boundary conditions, the equation admits a closed-form equilibrium solution given by the Boltzmann distribution

$$u_{\text{eq}}(x, y) = \frac{1}{Z} \exp(-V(x, y)), \tag{30}$$

where $Z = \int_{\Omega} \exp(-V(x, y)) dx dy$ ensures normalization. This analytical equilibrium solution is used solely for evaluation.

To approximate the equilibrium distribution, we employ a U-Net model with one input and one output channel. The input consists of normalized constant images corresponding to randomly sampled values of $\alpha \in [1, 2]$, with 256 distinct parameter instances used during training. The U-Net architecture contains three down- and up-sampling stages with channel widths (64, 128, 256) and produces outputs on a 32×32 grid. The network output represents cell-averaged initial conditions for the numerical solver.

A finite volume method (FVM) solver is then applied to advance these initial conditions toward equilibrium. We discretize Ω using a uniform 32×32 Cartesian grid. Diffusive fluxes are approximated with second-order central differences, while convective terms are treated using an exponential scheme to ensure numerical stability. Time integration is performed using a semi-implicit method with time step $\Delta t = 1/32$. For each training sample, the solver is executed for $N_s = 10$ iterations, which is sufficient due to the rapid relaxation of the system toward equilibrium under the chosen discretization. Mass conservation is enforced by the conservative FVM formulation.

Training is performed with a batch size of 64 and a learning rate of 10^{-4} with cosine-annealing Loshchilov & Hutter (2017) for 1000 epochs on a single NVIDIA A6000 GPU.

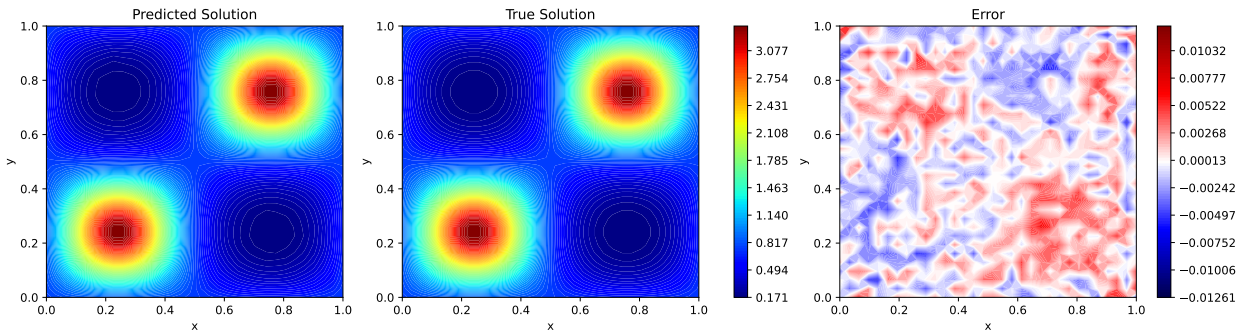


Figure 2: Predicted and true equilibrium solutions (left) and pointwise error (right) for $V(x, y) = 1.5 \sin(2\pi x) \sin(2\pi y)$.

As shown in Figure 2, the predicted solution closely matches the analytical equilibrium distribution, with pointwise errors on the order of 10^{-3} . Over the full parameter range, the L^2 error between the predicted and analytical solutions remains below 5×10^{-3} for most values of α , as summarized in Figure 6.

3.2 The 2D Lid-Driven Cavity using the Finite Element Method (FEM)

Forward problem. The two-dimensional lid-driven cavity is a classical benchmark problem in computational fluid dynamics (Ghia et al., 1982; Erturk et al., 2005). The system consists of a unit square cavity filled with an incompressible fluid, where the top lid moves at a constant unit velocity while the remaining walls are stationary. For Reynolds numbers in the range $Re \in [2000, 3000]$, the flow converges to a steady but strongly nonlinear regime characterized by multiple corner vortices and complex recirculation patterns (Arun & Satheesh, 2015; Arumuga Perumal & Dass, 2011). Despite its simple geometry, this regime is challenging for data-driven solvers due to the dominance of advection and the presence of sharp velocity gradients.

The flow is governed by the incompressible Navier–Stokes equations,

$$\frac{\partial \mathbf{u}}{\partial t} + (\mathbf{u} \cdot \nabla) \mathbf{u} = -\nabla P + \frac{1}{Re} \nabla^2 \mathbf{u}, \quad \nabla \cdot \mathbf{u} = 0, \quad (31)$$

where $\mathbf{u}(\mathbf{x}, t) = (u(\mathbf{x}, t), v(\mathbf{x}, t))$ is the velocity field and $P(\mathbf{x}, t)$ is the pressure. No-slip boundary conditions are imposed on all walls, with $\mathbf{u} = (1, 0)$ prescribed on the top lid and $\mathbf{u} = (0, 0)$ on the remaining boundaries. The steady-state solution corresponds to the time-independent form of (31).

Traditional physics-informed neural networks are known to struggle in this non-laminar regime for Reynolds numbers of this magnitude (Cao & Zhang, 2025). To address this limitation, we employ the NewPINNs framework by coupling a U-Net architecture with a high-fidelity finite element solver. The U-Net serves as a parameter-to-state initializer, while the numerical solver enforces the governing equations and boundary conditions.

The neural network follows a standard U-Net architecture with one input channel corresponding to the Reynolds number and three output channels corresponding to the velocity components (u, v) and pressure P . The network contains three down- and up-sampling stages with channel widths (64, 128, 256). Training inputs consist of normalized constant images constructed from 256 randomly sampled values of $Re \in [2000, 3000]$. The model is trained using the AdamW optimizer with a learning rate of 10^{-5} and a batch size of 64 for 300 epochs on a single NVIDIA A100 GPU.

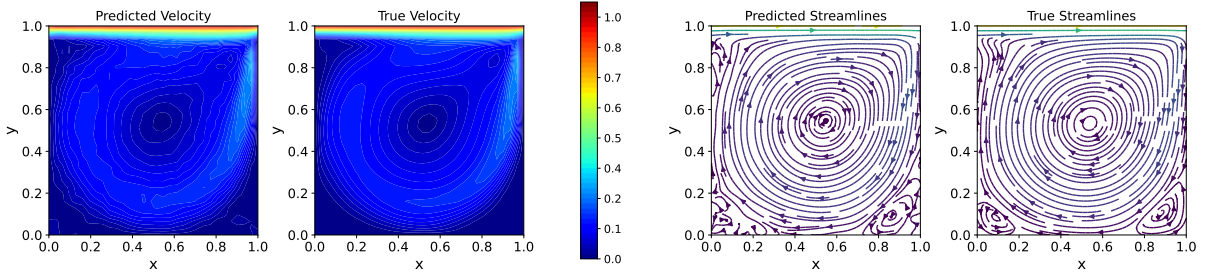


Figure 3: Predicted and true steady-state velocity fields (left) and streamlines (right) for $Re = 2500$.

The numerical solver is based on the finite element method, which discretizes the domain into triangular elements and approximates the solution using piecewise polynomial basis functions (Susanne C. Brenner, 2008). We employ a mesh consisting of triangular elements (with a maximum mesh spacing of 0.05), with cubic shape functions for the velocity and quadratic shape functions for the pressure to satisfy the inf-sup stability condition. Time integration is performed using a semi-implicit IMEX scheme with a time step size of 3×10^{-3} (Boscarino et al., 2024). For each input configuration, the solver is executed for $N_s = 500$ iterations, which is sufficient to converge to a steady-state solution.

To interface the convolutional network output with the finite element solver, we use the built-in `VoxelCoefficient` functionality in NGSolve, which maps grid-based (i.e. the U-net output) predictions onto the finite element mesh using polynomial interpolation for both training and inference.

As shown in Figure 3, the predicted velocity field closely matches the reference solution, accurately capturing the primary recirculation as well as the secondary vortex in the bottom-right corner. For $Re = 2500$, the mean squared errors for the velocity and pressure fields are 8.3×10^{-5} and 3.3×10^{-5} , respectively. Additional implementation details and quantitative results are provided in Appendix A.2.

3.3 Smooth Transient Dynamics: The 1D Allen–Cahn Equation using Chebfun

Forward problem. We next evaluate the ability of NewPINNs to handle nonlinear reaction–diffusion equations with smooth transient dynamics and periodic boundary conditions. The Allen–Cahn equation is a nonlinear parabolic PDE that arises in phase-field models of alloy decomposition, crystal growth, and interfacial motion (Kim et al., 2020). Its cubic reaction term introduces stiffness and strong nonlinearity, making it a challenging test case for purely data-driven approaches.

We consider the one-dimensional Allen–Cahn equation

$$\frac{\partial u}{\partial t} - \alpha \frac{\partial^2 u}{\partial x^2} + 5u^3 - 5u = 0, \quad x \in [-1, 1], \quad t \in [0, 1], \quad (32)$$

Table 1: Inverse Allen–Cahn parameter identification results ($\times 10^{-4}$).

True α	Predicted α (no noise)	Predicted α (10% noise)
1.00	(0.80 ± 0.35)	(0.71 ± 0.32)
4.00	(3.83 ± 0.15)	(3.79 ± 0.14)
7.00	(6.91 ± 0.11)	(6.86 ± 0.12)

where the diffusion coefficient $\alpha \in [10^{-4}, 10^{-3}]$. The initial condition is given by

$$u(x, 0) = x^2 \cos(\pi x),$$

and periodic boundary conditions are imposed,

$$u(1, t) = u(-1, t), \quad u_x(1, t) = u_x(-1, t).$$

To generate high-fidelity reference solutions, we employ the Chebfun package in MATLAB, which is a spectral solver that represents functions using Chebyshev polynomial interpolants (Driscoll et al., 2014). Periodicity and smoothness are handled intrinsically by the solver, eliminating the need for explicit boundary-condition enforcement or residual-based penalties in the learning process.

The learning task consists of approximating the spatiotemporal solution map $u(x, t)$ over the prescribed parameter and domain ranges. We use a fully connected neural network with five hidden layers of width 64 and hyperbolic tangent activation functions. The network is trained in a solver-coupled manner, where Chebfun enforces the governing dynamics and boundary conditions while the neural network learns a smooth representation of the solution consistent with the solver output.

Figure 4 compares the network predictions with the Chebfun solutions at multiple time instances. The results demonstrate close agreement throughout the temporal evolution.

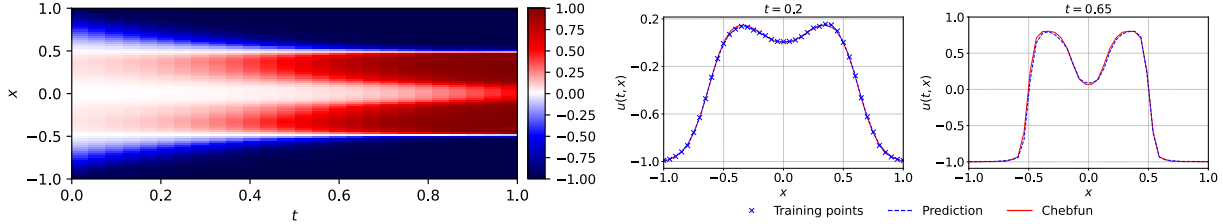


Figure 4: Allen–Cahn equation with $\alpha = 10^{-3}$. Left: Neural network prediction over the full space–time domain. Right: Network prediction at $t = 0.2$ with training points highlighted, and comparison between the network and solver solutions at $t = 0.65$.

Inverse problem. We also apply the NewPINNs framework to an inverse problem, where the goal is to identify the diffusion coefficient α in (32) from observed solution data. We consider two scenarios: noiseless measurements and measurements corrupted with 10% additive noise. In the forward loop, candidate values of α are sampled from the interval $[10^{-4}, 10^{-3}]$, which is chosen to reflect the physically relevant regime of interest.

Table 1 reports the inferred values of α for several ground-truth cases. The reported errors correspond to the standard deviation over five independent runs. The results indicate that the correct parameter is accurately recovered in the noiseless case and remains robust under moderate noise contamination, with only small deviations from the true value. Additional details and extended results are provided in Appendix A.3.

3.4 Chaotic Transient Systems: The 1D Kuramoto–Sivashinsky Equation using Chebfun

Forward problem. We next consider the Kuramoto–Sivashinsky (KS) equation, a canonical example of a nonlinear PDE exhibiting deterministic chaos and complex spatiotemporal behavior. The KS equa-

tion arises in a variety of physical contexts, including flame-front instabilities, thin liquid film flows, and interfacial turbulence models (Hoyle, 2006). Due to its combination of nonlinear advection, destabilizing low-order diffusion, and stabilizing fourth-order dissipation, the equation exhibits sensitive dependence on initial conditions and rapid error growth, making it a challenging benchmark for data-driven solvers.

We study the one-dimensional Kuramoto–Sivashinsky equation

$$\frac{\partial u}{\partial t} + u \frac{\partial u}{\partial x} + \alpha \frac{\partial^2 u}{\partial x^2} + \frac{\partial^4 u}{\partial x^4} = 0, \quad x \in [0, 100], \quad t \in [0, 20], \quad (33)$$

where $\alpha \in [1, 1.5]$. The initial condition is given by

$$u(x, 0) = \cos\left(\frac{x}{16}\right)\left(1 + \sin\left(\frac{x}{16}\right)\right),$$

and periodic boundary conditions are imposed on the spatial domain.

Standard physics-informed neural networks are known to struggle for this problem setting due to the chaotic nature of the dynamics and the presence of high-order derivatives (Wang et al., 2024b; Rout, 2023). Following the same strategy as in the Allen–Cahn experiment, we employ the Chebfun package in MATLAB as a high-accuracy spectral solver (Driscoll et al., 2014). Chebfun provides spectrally accurate spatial discretization and robust time integration while intrinsically enforcing periodicity.

The learning task is to approximate the spatiotemporal solution $u(x, t)$ over a finite time horizon, conditioned on the parameter α . We use a fully connected neural network with five hidden layers, each containing 64 neurons and hyperbolic tangent activation functions. The solver enforces the governing dynamics, while the neural network learns a smooth, solver-consistent representation of the evolving solution. Importantly, the objective is not long-term chaotic prediction, but accurate reproduction of the solution trajectory over the prescribed time window.

Figure 5 compares the neural network predictions with the Chebfun solutions at representative time instances for $\alpha = 1.1$. The results demonstrate close agreement, including accurate capture of sharp spatial transitions and rapidly evolving structures characteristic of the dynamics.

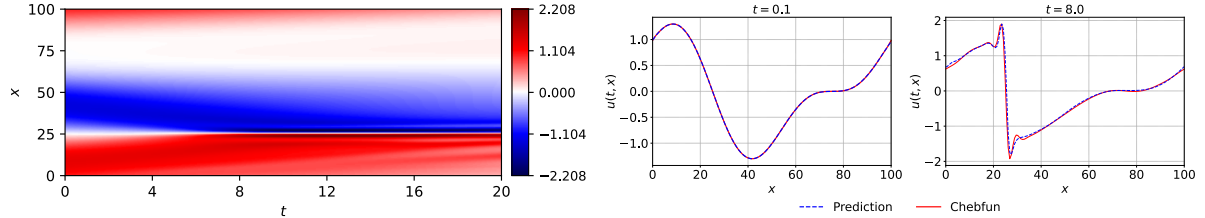


Figure 5: Kuramoto–Sivashinsky equation with $\alpha = 1.1$. Left: Neural network prediction over the full space–time domain. Right: Comparison between the neural network and solver solutions at $t = 0.1$ and $t = 8$.

Inverse problem. We also consider the inverse problem of identifying the parameter α in (33) from observed solution data. Using the inverse loop described in Algorithm 3, candidate values of α are sampled from the interval $[1, 1.5]$ and optimized to minimize the discrepancy between the model prediction and the measured data.

Table 2 reports the inferred values of α for both noiseless data and data contaminated with 10% additive noise. The reported uncertainties correspond to the standard deviation over five independent runs. The results indicate that the correct parameter is recovered with high accuracy in the noiseless case and remains robust under moderate noise, despite the chaotic nature of the underlying dynamics. Additional results and implementation details are provided in Appendix A.4.

Table 2: Inverse Kuramoto–Sivashinsky parameter identification results.

True α	Predicted α (no noise)	Predicted α (10% noise)
1.200	1.197 ± 0.012	1.187 ± 0.015
1.300	1.296 ± 0.010	1.289 ± 0.010
1.400	1.396 ± 0.010	1.391 ± 0.012

4 Limitations and Open Challenges

Although NewPINNs demonstrates strong performance across a range of forward and inverse problems, it is not without limitations. In systems exhibiting deterministic chaos, prediction accuracy degrades as trajectories evolve deeper into chaotic regimes. This behavior is observed in both the Kuramoto–Sivashinsky equation and the Lorenz system, where small discrepancies in the learned representation are rapidly amplified over time. Importantly, this degradation appears to stem from the intrinsic sensitivity of the underlying dynamics rather than from numerical instability or inaccuracies in the coupled solvers.

We hypothesize that this limitation is primarily tied to the representational capacity of the neural networks employed. Finite-capacity architectures may struggle to capture the fine-scale structures and rapid divergence of trajectories characteristic of strongly chaotic systems, particularly over long time horizons. While increasing model capacity or depth may improve expressiveness, it also introduces practical challenges, including overfitting, optimization instability, and increased computational cost. Whether alternative architectures, multiscale representations, or modified training strategies can systematically address these issues remains an open research question.

For higher-dimensional PDEs, additional challenges arise from the interaction between network initialization, normalization strategies, and solver stability. Because NewPINNs trains the neural network through a tight coupling with the numerical solver, poorly scaled or unstable network outputs can adversely affect solver convergence, particularly in stiff or highly nonlinear regimes. These effects are expected to become more pronounced for high-dimensional, chaotic, or turbulent flows.

Finally, it is important to emphasize that NewPINNs fundamentally inherits the accuracy and limitations of the underlying solver. Since the neural network is trained to emulate solver-consistent behavior, it cannot exceed the fidelity of the numerical method itself. As a result, improvements in solver accuracy, discretization quality, or numerical stability directly translate to improvements in the learned surrogate, while solver errors may propagate into the model predictions.

Overall, these observations highlight that while NewPINNs is effective across a broad class of problems, capturing long-term behavior in strongly chaotic and high-dimensional systems remains challenging. Understanding how architectural choices, solver fidelity, and training strategies interact in these regimes represents an important direction for future work.

5 Conclusion

We introduced NewPINNs, a hybrid learning framework that couples neural networks with classical numerical solvers to address forward and inverse problems governed by differential equations. In contrast to conventional physics-informed neural networks, which enforce governing equations and boundary conditions through loss-function penalties, NewPINNs delegates these responsibilities to external solvers. This separation simplifies the learning objective, improves training stability, and enables neural networks to function as solver-aware surrogate models.

Across a diverse set of benchmark problems such as steady-state flows, nonlinear reaction–diffusion systems, and chaotic transient dynamics, we demonstrated that NewPINNs produces accurate and physically consistent solutions. In particular, the framework remains effective in regimes where standard PINNs frequently struggle, such as high Reynolds number flows, stiff nonlinear dynamics, and chaotic systems over finite time horizons. By leveraging mature numerical solvers, NewPINNs naturally accommodates complex

boundary conditions, high-order operators, and multiscale phenomena without requiring problem-specific loss engineering.

While challenges remain for long-term prediction in strongly chaotic and high-dimensional systems, the results presented here suggest that solver-coupled learning provides a robust and flexible alternative to residual-based physics-informed approaches. We believe NewPINNs opens a promising direction for scalable and reliable physics-informed learning, with potential applications spanning computational physics, engineering, and scientific computing.

References

D. Arumuga Perumal and Anoop K. Dass. Multiplicity of steady solutions in two-dimensional lid-driven cavity flows by lattice boltzmann method. *Computers & Mathematics with Applications*, 61(12):3711–3721, 2011. ISSN 0898-1221. doi: <https://doi.org/10.1016/j.camwa.2010.03.053>. URL <https://www.sciencedirect.com/science/article/pii/S0898122110002427>. Mesoscopic Methods for Engineering and Science — Proceedings of ICMMES-09.

S. Arun and A. Satheesh. Analysis of flow behaviour in a two sided lid driven cavity using lattice boltzmann technique. *Alexandria Engineering Journal*, 54(4):795–806, 2015. ISSN 1110-0168. doi: <https://doi.org/10.1016/j.aej.2015.06.005>. URL <https://www.sciencedirect.com/science/article/pii/S1110016815000976>.

Uri M. Ascher and Linda R. Petzold. *Computer Methods for Ordinary Differential Equations and Differential-Algebraic Equations*. SIAM, 1998.

Mohammadmehdi Ataei and Hesam Salehipour. Xlb: A differentiable massively parallel lattice boltzmann library in python. *Computer Physics Communications*, 300:109187, 2024. ISSN 0010-4655. doi: <https://doi.org/10.1016/j.cpc.2024.109187>. URL <https://www.sciencedirect.com/science/article/pii/S0010465524001103>.

Shaojie Bai, J. Zico Kolter, and Vladlen Koltun. Deep equilibrium models, 2019. URL <https://arxiv.org/abs/1909.01377>.

Shaojie Bai, Vladlen Koltun, and J. Zico Kolter. Multiscale deep equilibrium models, 2020. URL <https://arxiv.org/abs/2006.08656>.

Klaus-Jürgen Bathe. *Finite Element Procedures*. Klaus-Jürgen Bathe, 2006.

J. Blazek. *Computational Fluid Dynamics: Principles and Applications*. Elsevier, 3 edition, 2015. ISBN 9780127999144.

Sebastiano Boscarino, Lorenzo Pareschi, and Giovanni Russo. *Implicit-Explicit Methods for Evolutionary Partial Differential Equations*. Society for Industrial and Applied Mathematics, Philadelphia, PA, 2024. doi: 10.1137/1.9781611978209. URL <https://pubs.siam.org/doi/abs/10.1137/1.9781611978209>.

Jean Bourgain and Nataša Pavlović. Ill-posedness of the navier–stokes equations in a critical space in 3d. *Journal of Functional Analysis*, 255(9):2233–2247, 2008. ISSN 0022-1236. doi: <https://doi.org/10.1016/j.jfa.2008.07.008>. URL <https://www.sciencedirect.com/science/article/pii/S0022123608002723>. Special issue dedicated to Paul Malliavin.

Samira Boussaid, Danielle Hilhorst, and Thanh Nguyen. Convergence to steady state for the solutions of a nonlocal reaction-diffusion equation. *Evolution Equations and Control Theory*, 4:39–59, 03 2015. doi: 10.3934/eect.2015.4.39.

Steven L. Brunton, Joshua L. Proctor, and J. Nathan Kutz. Sparse identification of nonlinear dynamics with control (sindyc). *IFAC-PapersOnLine*, 49(18):710–715, 2016. ISSN 2405-8963. doi: <https://doi.org/10.1016/j.ifacol.2016.10.249>. URL <https://www.sciencedirect.com/science/article/pii/S2405896316318298>. 10th IFAC Symposium on Nonlinear Control Systems NOLCOS 2016.

Wenbo Cao and Weiwei Song, Jiahaoand Zhang. A solver for subsonic flow around airfoils based on physics-informed neural networks and mesh transformation. *Physics of Fluids*, 36(2):027134, 02 2024. ISSN 1070-6631. doi: 10.1063/5.0188665. URL <https://doi.org/10.1063/5.0188665>.

Wenbo Cao and Weiwei Zhang. An analysis and solution of ill-conditioning in physics-informed neural networks. *Journal of Computational Physics*, 520:113494, 2025. ISSN 0021-9991. doi: <https://doi.org/10.1016/j.jcp.2024.113494>. URL <https://www.sciencedirect.com/science/article/pii/S0021999124007423>.

Junfeng Chen and Kailiang Wu. Deep-osg: Deep learning of operators in semigroup. *Journal of Computational Physics*, 493:112498, 2023. ISSN 0021-9991. doi: <https://doi.org/10.1016/j.jcp.2023.112498>. URL <https://www.sciencedirect.com/science/article/pii/S0021999123005934>.

Ricky T. Q. Chen, Yulia Rubanova, Jesse Bettencourt, and David K Duvenaud. Neural ordinary differential equations. In S. Bengio, H. Wallach, H. Larochelle, K. Grauman, N. Cesa-Bianchi, and R. Garnett (eds.), *Advances in Neural Information Processing Systems*, volume 31. Curran Associates, Inc., 2018. URL https://proceedings.neurips.cc/paper_files/paper/2018/file/69386f6bb1dfed68692a24c8686939b9-Paper.pdf.

Steven M. Cox and Paul C. Matthews. Exponential time differencing for stiff systems. *Journal of Computational Physics*, 176(2):430–455, 2002.

Alban de Vaucorbeil, Vinh Phu Nguyen, Sina Sinaie, and Jian Ying Wu. Chapter two - material point method after 25 years: Theory, implementation, and applications. In Stéphane P.A. Bordas and Daniel S. Balint (eds.), *Chapter Two - Material point method after 25 years: Theory, implementation, and applications*, volume 53 of *Advances in Applied Mechanics*, pp. 185–398. Elsevier, 2020. doi: <https://doi.org/10.1016/bs.aams.2019.11.001>. URL <https://www.sciencedirect.com/science/article/pii/S0065215619300146>.

T. A Driscoll, N. Hale, and L. N. Trefethen. *Chebfun Guide*. Pafnuty Publications, 2014. URL <http://www.chebfun.org/docs/guide/>.

Clive L. Dym and Irving H. Shames. *Solid Mechanics: A Variational Approach, Augmented Edition*. Springer New York, New York, NY, 2013. ISBN 978-1-4614-6033-6. doi: 10.1007/978-1-4614-6034-3. URL <https://link.springer.com/book/10.1007/978-1-4614-6034-3>.

Kevin Egan, Weizhen Li, and Rui Carvalho. Automatically discovering ordinary differential equations from data with sparse regression. *Communications Physics*, 7(1):20, January 2024. ISSN 2399-3650. doi: 10.1038/s42005-023-01516-2. URL <https://doi.org/10.1038/s42005-023-01516-2>.

E. Erturk, T. C. Corke, and C. Gökçöl. Numerical solutions of 2-d steady incompressible driven cavity flow at high reynolds numbers. *International Journal for Numerical Methods in Fluids*, 48(7):747–774, 2005. doi: <https://doi.org/10.1002/fld.953>. URL <https://onlinelibrary.wiley.com/doi/abs/10.1002/fld.953>.

Lawrence C. Evans. *Partial differential equations*. American Mathematical Society, Providence, R.I., 2010. ISBN 9780821849743 0821849743.

Mikihiro Fujii. Ill-posedness of the two-dimensional stationary navier–stokes equations on the whole plane. *Annals of PDE*, 10(1):10, May 2024. ISSN 2199-2576. doi: 10.1007/s40818-024-00174-z. URL <https://doi.org/10.1007/s40818-024-00174-z>.

Han Gao, Matthew J. Zahr, and Jian-Xun Wang. Physics-informed graph neural galerkin networks: A unified framework for solving pde-governed forward and inverse problems. *Computer Methods in Applied Mechanics and Engineering*, 390:114502, 2022. ISSN 0045-7825. doi: <https://doi.org/10.1016/j.cma.2021.114502>. URL <https://www.sciencedirect.com/science/article/pii/S0045782521007076>.

U Ghia, K.N Ghia, and C.T Shin. High-re solutions for incompressible flow using the navier-stokes equations and a multigrid method. *Journal of Computational Physics*, 48(3):387–411, 1982. ISSN 0021-9991. doi: [https://doi.org/10.1016/0021-9991\(82\)90058-4](https://doi.org/10.1016/0021-9991(82)90058-4). URL <https://www.sciencedirect.com/science/article/pii/0021999182900584>.

Irina Ginzburg. Two-relaxation-time lattice boltzmann scheme: about parametrization, velocity, pressure and mixed boundary conditions. *Communications in Computational Physics*, 3:427–478, 01 2008.

Andrzej Granas and James Dugundji. *Fixed Point Theory*. Springer Monographs in Mathematics. Springer, 2003. ISBN 978-0387001735. URL https://books.google.com/books/about/Fixed_Point_Theory.html?id=4_iJAAoLSq3cC.

Bertil Gustafsson, Heinz-Otto Kreiss, and Joseph Oliger. *Time-Dependent Problems and Difference Methods*. Pure and Applied Mathematics: A Wiley Series of Texts, Monographs and Tracts. John Wiley & Sons, Hoboken, NJ, 2 edition, 2013. ISBN 978-0-470-90056-7.

Kyle J. Haughey. Boundless fluids using the lattice-boltzmann method. Master’s thesis, California Polytechnic State University, San Luis Obispo, San Luis Obispo, CA, June 2009. URL <https://digitalcommons.calpoly.edu/theses/117/>.

Kaiming He, Xiangyu Zhang, Shaoqing Ren, and Jian Sun. Delving deep into rectifiers: Surpassing human-level performance on imagenet classification. In *Proceedings of the IEEE International Conference on Computer Vision (ICCV)*, pp. 1026–1034, 2015. doi: 10.1109/ICCV.2015.123.

S.A. Hosseini, M. Atif, S. Asumali, and I.V. Karlin. Entropic lattice boltzmann methods: A review. *Computers & Fluids*, 259:105884, 2023. ISSN 0045-7930. doi: <https://doi.org/10.1016/j.compfluid.2023.105884>. URL <https://www.sciencedirect.com/science/article/pii/S0045793023001093>.

Rebecca B. Hoyle. *Pattern Formation: An Introduction to Methods*. Cambridge University Press, Cambridge, UK, 2006. ISBN 9780521009760.

Yunfei Huang, Youssef Mabrouk, Gerhard Gompper, and Benedikt Sabass. Sparse inference and active learning of stochastic differential equations from data. *Scientific Reports*, 12(1):21691, Dec 2022. ISSN 2045-2322. doi: 10.1038/s41598-022-25638-9. URL <https://doi.org/10.1038/s41598-022-25638-9>.

J. D. Jackson. *Electrodynamics, Classical*. John Wiley & Sons, Ltd, 2003. ISBN 9783527600434. doi: <https://doi.org/10.1002/3527600434.eap109>. URL <https://onlinelibrary.wiley.com/doi/abs/10.1002/3527600434.eap109>.

Ameya D. Jagtap, Ehsan Kharazmi, and George Em Karniadakis. Conservative physics-informed neural networks on discrete domains for conservation laws: Applications to forward and inverse problems. *Computer Methods in Applied Mechanics and Engineering*, 365:113028, 2020. ISSN 0045-7825. doi: <https://doi.org/10.1016/j.cma.2020.113028>. URL <https://www.sciencedirect.com/science/article/pii/S0045782520302127>.

Weiwei Ji, Weilun Qiu, Zhiyu Shi, Shaowu Pan, and Sili Deng. Stiff-pinn: Physics-informed neural network for stiff chemical kinetics. *The Journal of Physical Chemistry A*, 125(36):8098–8106, 2021. doi: 10.1021/acs.jpca.1c05102. URL <https://doi.org/10.1021/acs.jpca.1c05102>. PMID: 34463510.

Ge Jin, Jian Cheng Wong, Abhishek Gupta, Shipeng Li, and Yew-Soon Ong. Fourier warm start for physics-informed neural networks. *Engineering Applications of Artificial Intelligence*, 132:107887, 2024. ISSN 0952-1976. doi: <https://doi.org/10.1016/j.engappai.2024.107887>. URL <https://www.sciencedirect.com/science/article/pii/S0952197624000459>.

Hyundong Kim, Sungha Yoon, Jian Wang, Chaeyoung Lee, Sangkwon Kim, Jintae Park, and Junseok Kim. Shape transformation using the modified allen-cahn equation. *Applied Mathematics Letters*, 107:106487, 2020. ISSN 0893-9659. doi: <https://doi.org/10.1016/j.aml.2020.106487>. URL <https://www.sciencedirect.com/science/article/pii/S0893965920302275>.

Jeongsu Lee. Anti-derivatives approximator for enhancing physics-informed neural networks. *Computer Methods in Applied Mechanics and Engineering*, 426:117000, 2024. ISSN 0045-7825. doi: <https://doi.org/10.1016/j.cma.2024.117000>. URL <https://www.sciencedirect.com/science/article/pii/S0045782524002561>.

Randall J. LeVeque. *Finite Volume Methods for Hyperbolic Problems*. Cambridge Texts in Applied Mathematics. Cambridge University Press, 2002.

Randall J. LeVeque. *Finite Difference Methods for Ordinary and Partial Differential Equations: Steady-State and Time-Dependent Problems*. Society for Industrial and Applied Mathematics, Philadelphia, PA, 2007a. ISBN 978-0-898716-29-0. doi: 10.1137/1.9780898717839.

Randall J. LeVeque. *Finite Difference Methods for Ordinary and Partial Differential Equations*. Society for Industrial and Applied Mathematics, 2007b. doi: 10.1137/1.9780898717839. URL <https://pubs.siam.org/doi/abs/10.1137/1.9780898717839>.

Randall J. LeVeque. *Finite Difference Methods for Ordinary and Partial Differential Equations: Steady-State and Time-Dependent Problems*. SIAM, 2007c.

Zongyi Li, Nikola B. Kovachki, Kamyar Azizzadenesheli, Burigede Liu, Kaushik Bhattacharya, Andrew M. Stuart, and Anima Anandkumar. Fourier neural operator for parametric partial differential equations. *CoRR*, abs/2010.08895, 2020. URL <https://arxiv.org/abs/2010.08895>.

Zichao Long, Yiping Lu, and Bin Dong. Pde-net 2.0: Learning pdes from data with a numeric-symbolic hybrid deep network. *Journal of Computational Physics*, 399:108925, 2019. ISSN 0021-9991. doi: <https://doi.org/10.1016/j.jcp.2019.108925>. URL <https://www.sciencedirect.com/science/article/pii/S0021999119306308>.

Ilya Loshchilov and Frank Hutter. Sgdr: Stochastic gradient descent with warm restarts, 2017. URL <https://arxiv.org/abs/1608.03983>.

Lu Lu, Pengzhan Jin, Guofei Pang, Zhongqiang Zhang, and George Em Karniadakis. Learning nonlinear operators via deeponet based on the universal approximation theorem of operators. *Nature Machine Intelligence*, 3(3):218–229, Mar 2021. ISSN 2522-5839. doi: 10.1038/s42256-021-00302-5. URL <https://doi.org/10.1038/s42256-021-00302-5>.

Tanya Marwah, Ashwini Pokle, J Zico Kolter, Zachary Chase Lipton, Jianfeng Lu, and Andrej Risteski. Deep equilibrium based neural operators for steady-state PDEs. In *Thirty-seventh Conference on Neural Information Processing Systems*, 2023. URL <https://openreview.net/forum?id=v6YzxwJ1Qn>.

Fredrik Bengzon Mats G. Larson. *The Finite Element Method: Theory, Implementation, and Applications*. Springer Berlin, Heidelberg, 2013.

Kazem Meidani and Amir Barati Farimani. Data-driven identification of 2d partial differential equations using extracted physical features. *Computer Methods in Applied Mechanics and Engineering*, 381:113831, 2021. ISSN 0045-7825. doi: <https://doi.org/10.1016/j.cma.2021.113831>. URL <https://www.sciencedirect.com/science/article/pii/S0045782521001687>.

J.-P. Merlet. Mixing neural networks, continuation and symbolic computation to solve parametric systems of non linear equations. *Neural Networks*, 176:106316, 2024. ISSN 0893-6080. doi: <https://doi.org/10.1016/j.neunet.2024.106316>. URL <https://www.sciencedirect.com/science/article/pii/S0893608024002405>.

Abdul Hannan Mustajab, Hao Lyu, Zarghaam Rizvi, and Frank Wuttke. Physics-informed neural networks for high-frequency and multi-scale problems using transfer learning. *Applied Sciences*, 14(8), 2024. ISSN 2076-3417. doi: 10.3390/app14083204. URL <https://www.mdpi.com/2076-3417/14/8/3204>.

Vinh Phu Nguyen, Alban de Vaucoubeil, and Stephane Bordas. *The Material Point Method*. Scientific Computation. Springer Cham, 1 edition, 2023. ISBN 978-3-031-24069-0. doi: 10.1007/978-3-031-24070-6. URL <https://doi.org/10.1007/978-3-031-24070-6>. Hardcover published: 12 April 2023; eBook published: 11 April 2023; Softcover published: 13 April 2024.

Vivek Oommen, Khemraj Shukla, Saaketh Desai, Rémi Dingreville, and George Em Karniadakis. Rethinking materials simulations: Blending direct numerical simulations with neural operators. *npj Computational Materials*, 10(1):145, July 2024. ISSN 2057-3960. doi: 10.1038/s41524-024-01319-1. URL <https://doi.org/10.1038/s41524-024-01319-1>.

Ronald L. Panton. *Incompressible Flow*. John Wiley & Sons, Ltd, 2013. ISBN 9781118013434.

Jun-Cai Pu and Yong Chen. Data-driven forward-inverse problems for yajima–oikawa system using deep learning with parameter regularization. *Communications in Nonlinear Science and Numerical Simulation*, 118:107051, 2023. ISSN 1007-5704. doi: <https://doi.org/10.1016/j.cnsns.2022.107051>. URL <https://www.sciencedirect.com/science/article/pii/S100757042200538X>.

Chris Rackauckas, Yingbo Ma, Julius Martensen, Collin Warner, Kirill Zubov, Rohit Supekar, Dominic Skinner, and Ali Ramadhan. Universal differential equations for scientific machine learning. *ArXiv*, 01 2020. doi: 10.21203/rs.3.rs-55125/v1.

M. Raissi, P. Perdikaris, and G.E. Karniadakis. Physics-informed neural networks: A deep learning framework for solving forward and inverse problems involving nonlinear partial differential equations. *Journal of Computational Physics*, 378:686–707, 2019. ISSN 0021-9991. doi: <https://doi.org/10.1016/j.jcp.2018.10.045>. URL <https://www.sciencedirect.com/science/article/pii/S0021999118307125>.

Maziar Raissi. Deep hidden physics models: Deep learning of nonlinear partial differential equations. *Journal of Machine Learning Research*, 19, 01 2018. doi: 10.48550/arXiv.1801.06637.

Maziar Raissi, Alireza Yazdani, and George Em Karniadakis. Hidden fluid mechanics: Learning velocity and pressure fields from flow visualizations. *Science*, 367(6481):1026–1030, 2020. doi: 10.1126/science.aaw4741. URL <https://www.science.org/doi/abs/10.1126/science.aaw4741>.

Pratik Rathore, Weimu Lei, Zachary Frangella, Lu Lu, and Madeleine Udell. Challenges in training pinns: a loss landscape perspective. In *Proceedings of the 41st International Conference on Machine Learning, ICML’24*. JMLR.org, 2024.

Siddharth Rout. Pinn for dynamical partial differential equations is not training deeper networks rather learning advection and time variance, 2023. URL <https://arxiv.org/abs/2301.04793>.

Yanjie Song, He Wang, He Yang, Maria Luisa Taccari, and Xiaohui Chen. Loss-attentional physics-informed neural networks. *Journal of Computational Physics*, 501:112781, 2024. ISSN 0021-9991. doi: <https://doi.org/10.1016/j.jcp.2024.112781>. URL <https://www.sciencedirect.com/science/article/pii/S0021999124000305>.

H Steven. Strogatz, nonlinear dynamics and chaos, 2015.

Vidar Thomée Stig Larsson. *Partial Differential Equations with Numerical Methods*. Springer Berlin, Heidelberg, 2003.

L. Ridgway Scott Susanne C. Brenner. *The Mathematical Theory of Finite Element Methods*. Springer New York, NY, 2008.

Kianoosh Taghikhani, Yusuke Yamazaki, Jerry Paul Varghese, Markus Apel, Reza Najian Asl, and Shahed Rezaei. Neural-initialized newton: Accelerating nonlinear finite elements via operator learning, 2025. URL <https://arxiv.org/abs/2511.06802>.

Lloyd N. Trefethen. *Spectral Methods in MATLAB*. SIAM, 2000.

Lloyd N. Trefethen et al. *Exploring the Chebfun System*. The Chebfun Development Team, 2014. URL <https://www.chebfun.org/docs/guide/>. Chapter 11.

Tai-Peng Tsai. *Lectures on Navier-Stokes equations*. Graduate Studies in Mathematics,. American Mathematical Society,, Providence, R.I. :, 2018. URL <https://doi.org/10.1090/gsm/192>.

Pauli Virtanen, Ralf Gommers, Travis E. Oliphant, Matt Haberland, Tyler Reddy, David Cournapeau, Evgeni Burovski, Pearu Peterson, Warren Weckesser, Jonathan Bright, et al. Scipy 1.0: Fundamental algorithms for scientific computing in python. *Nature Methods*, 17:261–272, 2020.

Sifan Wang, Yujun Teng, and Paris Perdikaris. Understanding and mitigating gradient flow pathologies in physics-informed neural networks. *SIAM Journal on Scientific Computing*, 43:A3055–A3081, 09 2021. doi: 10.1137/20M1318043.

Sifan Wang, Shyam Sankaran, and Paris Perdikaris. Respecting causality for training physics-informed neural networks. *Computer Methods in Applied Mechanics and Engineering*, 421:116813, 2024a. ISSN 0045-7825. doi: <https://doi.org/10.1016/j.cma.2024.116813>. URL <https://www.sciencedirect.com/science/article/pii/S0045782524000690>.

Sifan Wang, Shyam Sankaran, and Paris Perdikaris. Respecting causality for training physics-informed neural networks. *Computer Methods in Applied Mechanics and Engineering*, 421:116813, 2024b. ISSN 0045-7825. doi: <https://doi.org/10.1016/j.cma.2024.116813>. URL <https://www.sciencedirect.com/science/article/pii/S0045782524000690>.

Yizheng Wang, Zhongkai Hao, Mohammad Sadegh Eshaghi, Cosmin Anitescu, Xiaoying Zhuang, Timon Rabczuk, and Yinghua Liu. Pretrain finite element method: A pretraining and warm-start framework for pdes via physics-informed neural operators, 2026. URL <https://arxiv.org/abs/2601.03086>.

Ezra Winston and J. Zico Kolter. Monotone operator equilibrium networks, 2021. URL <https://arxiv.org/abs/2006.08591>.

H. Xu, J. Zeng, and D. Zhang. Discovery of partial differential equations from highly noisy and sparse data with physics-informed information criterion. *Research*, 6:0147, May 2023. doi: 10.34133/research.0147.

Fan Yang, Hao Liu, Xiao-Xiao Li, and Jian-Xiong Cao. Pinn neural network method for solving the forward and inverse problem of time-fractional telegraph equation. *Results in Engineering*, 25:103997, 2025. ISSN 2590-1230. doi: <https://doi.org/10.1016/j.rineng.2025.103997>. URL <https://www.sciencedirect.com/science/article/pii/S2590123025000854>.

Xin Ye, Yi-Qing Ni, Wai Kei Ao, and Lei Yuan. Modeling of the hysteretic behavior of nonlinear particle damping by fourier neural network with transfer learning. *Mechanical Systems and Signal Processing*, 208:111006, 2024. ISSN 0888-3270. doi: <https://doi.org/10.1016/j.ymssp.2023.111006>. URL <https://www.sciencedirect.com/science/article/pii/S0888327023009147>.

Enrui Zhang, Adar Kahana, Alena Kopaničáková, Eli Turkel, Rishikesh Ranade, Jay Pathak, and George Em Karniadakis. Blending neural operators and relaxation methods in pde numerical solvers. *Nature Machine Intelligence*, 6(11):1303–1313, November 2024. ISSN 2522-5839. doi: 10.1038/s42256-024-00910-x. URL <https://doi.org/10.1038/s42256-024-00910-x>.

Chi Zhao, Feifei Zhang, Wenqiang Lou, Xi Wang, and Jianyong Yang. A comprehensive review of advances in physics-informed neural networks and their applications in complex fluid dynamics. *Physics of Fluids*, 36(10):101301, 10 2024. ISSN 1070-6631. doi: 10.1063/5.0226562. URL <https://doi.org/10.1063/5.0226562>.

Bohong Zheng. Ordinary differential equation and its application. *Highlights in Science, Engineering and Technology*, 72:645–651, 12 2023. doi: 10.54097/rnnev212.

A Experimental Details

A.1 2D Fokker–Planck Equation using the Finite Volume Method

Problem statement. We consider the two-dimensional Fokker–Planck equation posed on the unit square domain $\Omega = [0, 1]^2$,

$$\frac{\partial u}{\partial t} = \nabla \cdot (\nabla u + u \nabla V), \quad (x, y) \in \Omega, \quad (34)$$

where $u(x, y, t)$ denotes a probability density and the potential $V(x, y)$ is parameterized by

$$V(x, y) = \alpha \sin(2\pi x) \sin(2\pi y), \quad \alpha \in [1, 2]. \quad (35)$$

No-flux boundary conditions are imposed on $\partial\Omega$, ensuring conservation of total probability.

For confining potentials of this form, the system converges to a unique steady-state equilibrium distribution given by the Boltzmann density

$$u_{\text{eq}}(x, y) = \frac{1}{Z} \exp(-V(x, y)), \quad Z = \int_{\Omega} \exp(-V(x, y)) dx dy, \quad (36)$$

which is used solely for evaluation and error analysis.

Numerical solver. Reference solutions are generated using a finite volume method (FVM), which enforces the governing equation in integral form over a collection of control volumes. The domain Ω is discretized using a uniform Cartesian grid with 32×32 square cells. Cell averages of u are evolved in time by balancing diffusive and convective fluxes across cell faces.

Diffusive fluxes are approximated using second-order central differences. The drift term $u \nabla V$ is treated using an exponential fitting scheme, which improves numerical stability in convection-dominated regimes and preserves positivity of the density. Time integration is performed using a semi-implicit scheme with time step $\Delta t = 1/32$. For each solver call during training, the system is advanced for $N_s = 10$ time steps, which is sufficient to significantly reduce transients while remaining computationally inexpensive.

The conservative structure of the finite volume discretization ensures mass conservation up to solver tolerances throughout training.

Training NewPINNs. The neural network is a U-Net architecture with a single input channel corresponding to the scalar parameter α and a single output channel representing the spatial distribution of u on a 32×32 grid. The U-Net contains three downsampling and upsampling stages with channel widths (64, 128, 256).

Training inputs consist of normalized constant images constructed from 256 uniformly sampled values of $\alpha \in [1, 2]$. For each parameter value, the network produces a candidate equilibrium density $u_{\text{grid}}(\alpha)$, which is interpreted as a set of cell averages and passed directly to FiPy as an initial condition. The solver advances this state for N_s iterations, producing $u_{\text{solver}}(\alpha)$.

The loss function is defined as the mean-squared discrepancy between the network output and the solver-advanced state,

$$\mathcal{L}(\theta) = \frac{1}{N_{\alpha}} \sum_{\alpha} \|u_{\text{grid}}(\alpha; \theta) - u_{\text{solver}}(\alpha)\|_{L^2(\Omega)}^2, \quad (37)$$

which enforces fixed-point consistency of the learned solution under the solver dynamics.

Training is performed using a batch size of 64 and a learning rate of 10^{-4} for 1000 epochs on a single NVIDIA A6000 GPU. Cosine annealing is applied to the learning rate schedule to improve convergence stability with the loss converging to the order of 10^{-4} as shown in Figure 6.

Stability and initialization considerations. Since the neural network output is used as a virtual initial condition for the finite volume solver, initialization plays a critical role in training stability. We observe that standard Kaiming initialization produces sufficiently smooth and bounded outputs to ensure solver convergence throughout training. Aggressive initialization or excessively large solver iteration counts can lead to transient instabilities or slow convergence, although such behavior was not observed for the parameter range considered here.

Experimental results. Across the full parameter range $\alpha \in [1, 2]$, the learned equilibrium densities closely match the analytical Boltzmann solutions. Pointwise errors are typically on the order of 10^{-3} , and the L^2 error remains below 5×10^{-3} for most parameter values as shown in Figure 6. Thus, the network successfully captures both the spatial structure and amplitude variation induced by changes in α , demonstrating that NewPINNs can accurately learn steady-state solutions governed by finite volume discretizations.

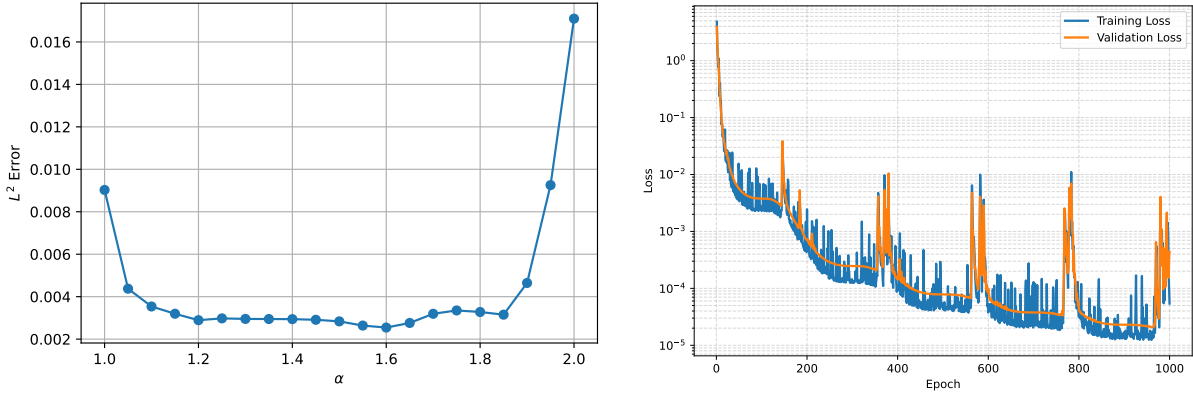


Figure 6: The L^2 error of the predicted Fokker-Planck solution (left) and the loss function plot (right).

A.2 2D Lid-Driven Cavity using the Finite Element Method

Problem statement. We consider the two-dimensional lid-driven cavity problem governed by the incompressible Navier–Stokes equations

$$\frac{\partial \mathbf{u}}{\partial t} + (\mathbf{u} \cdot \nabla) \mathbf{u} = -\nabla P + \frac{1}{\text{Re}} \nabla^2 \mathbf{u}, \quad \nabla \cdot \mathbf{u} = 0, \quad (38)$$

with boundary conditions

$$\mathbf{u} = (1, 0) \quad \text{on } \Gamma_0, \quad \mathbf{u} = (0, 0) \quad \text{on } \Gamma_1,$$

where Γ_0 denotes the top moving lid and Γ_1 denotes the remaining three stationary walls. The solution consists of the velocity field $\mathbf{u}(\mathbf{x}, t) = (u(\mathbf{x}, t), v(\mathbf{x}, t))$ and pressure field $P(\mathbf{x}, t)$.

Since our objective is to approximate steady-state solutions, we focus on the time-independent equilibrium reached by the system for Reynolds numbers $\text{Re} \in [2000, 3000]$. From a learning perspective, this allows the problem to be cast as a parameter-to-solution map, motivating the use of a U-Net architecture as described in the main text.

Numerical solver. We employ the finite element method (FEM) implemented in NGSolve to compute reference solutions. The spatial domain is discretized using a triangular mesh generated via NGSolve’s `Mesh` function, with a prescribed maximum global mesh size of $h_{\max} = 0.05$.

The velocity and pressure fields are approximated as

$$u(\mathbf{x}, t) \approx \sum_{i=1}^N u_i(t) \phi_i(\mathbf{x}), \quad v(\mathbf{x}, t) \approx \sum_{i=1}^N v_i(t) \phi_i(\mathbf{x}), \quad P(\mathbf{x}, t) \approx \sum_{i=1}^N P_i(t) \varphi_i(\mathbf{x}), \quad (39)$$

where ϕ_i are piecewise cubic basis functions for the velocity and φ_i are piecewise quadratic basis functions for the pressure. This choice satisfies the inf–sup stability condition. Time integration is performed using an implicit–explicit (IMEX) scheme with time step size $\Delta t = 3 \times 10^{-3}$ (Stig Larsson, 2003). The solver is iterated until a steady state is reached.

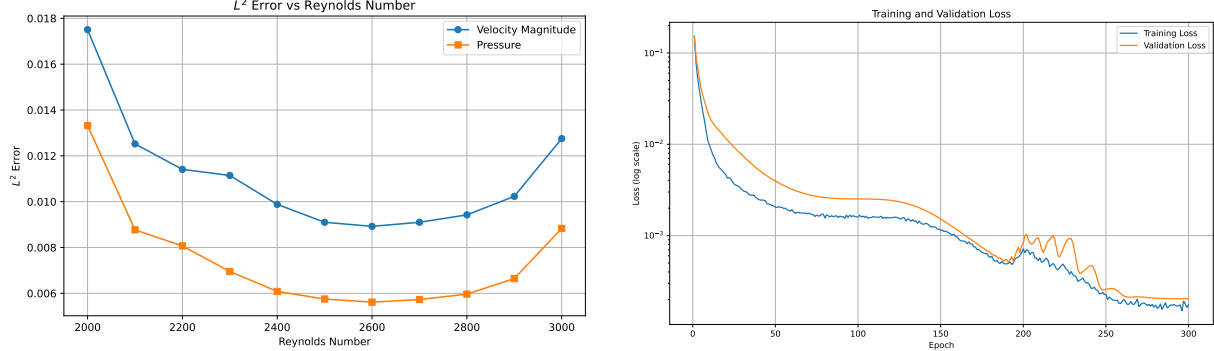


Figure 7: The L^2 error of the velocity magnitude and the pressure vs the Reynold’s number and the loss function plot (right).

Training NewPINNs. The U-Net architecture consists of a single input channel corresponding to the Reynolds number and three output channels corresponding to the velocity components and pressure, discretized on a 32×32 Cartesian grid:

$$\hat{u}_{\text{grid}}(\mathbf{x}), \hat{v}_{\text{grid}}(\mathbf{x}), \hat{P}_{\text{grid}}(\mathbf{x}) = f_{\text{NN}}(\text{Re}; \theta). \quad (40)$$

For notational simplicity, the explicit dependence on Re is omitted in subsequent expressions.

To interface the grid-based network outputs with the FEM solver, we employ NGSolve’s `VoxelCoefficient` functionality, which linearly interpolates grid values onto the finite element mesh:

$$\hat{u}_{\text{FEM}}, \hat{v}_{\text{FEM}}, \hat{P}_{\text{FEM}} = \text{VoxelCoefficient}(\hat{u}_{\text{grid}}, \hat{v}_{\text{grid}}, \hat{P}_{\text{grid}}). \quad (41)$$

These interpolated fields are then used as initial conditions for the FEM solver, which is executed for $N_s = 500$ iterations:

$$(u_{\text{FEM}}^*, v_{\text{FEM}}^*, P_{\text{FEM}}^*) = \mathcal{S}(\hat{u}_{\text{FEM}}, \hat{v}_{\text{FEM}}, \hat{P}_{\text{FEM}}, \text{Re}, N_s). \quad (42)$$

The resulting FEM solutions are mapped back to the 32×32 grid by direct evaluation on an evenly spaced lattice,

$$(u_{\text{grid}}^*, v_{\text{grid}}^*, P_{\text{grid}}^*) = \text{GridEvaluation}(u_{\text{FEM}}^*, v_{\text{FEM}}^*, P_{\text{FEM}}^*). \quad (43)$$

The training loss is defined as the averaged L^2 discrepancy between the network predictions and the solver outputs over a batch of Reynolds numbers:

$$\mathcal{L}(\theta) = \frac{1}{M} \sum_{\text{Re}} \left(\|\hat{u}_{\text{grid}} - u_{\text{grid}}^*\|_{L^2(\Omega)}^2 + \|\hat{v}_{\text{grid}} - v_{\text{grid}}^*\|_{L^2(\Omega)}^2 + \|\hat{P}_{\text{grid}} - P_{\text{grid}}^*\|_{L^2(\Omega)}^2 \right), \quad (44)$$

where M is the batch size. This formulation decouples the neural network from a fixed mesh resolution. In practice, however, meaningful interpolation requires that the grid resolution of the U-Net output be comparable to the FEM mesh density.

Initialization and stability considerations. A critical practical consideration is the initialization of the neural network. PDE solvers admit stable solutions only for restricted classes of initial conditions (Bourgain & Pavlović, 2008; Fujii, 2024). When the output of an untrained network is used as a virtual initial condition, the solver may fail to converge or produce invalid values.

We observe that the default Kaiming initialization (gain = 1.0) used in the HuggingFace U-Net implementation is generally sufficient for stable training (He et al., 2015). However, increasing the initialization gain or extending the solver iteration count (e.g., from 500 to 1000 iterations) can lead to solver breakdowns, manifested as `NaN` or `Inf` values. These issues are expected to become more pronounced for higher-dimensional or more chaotic flow regimes.

Experimental results. Validation losses are computed using mean-squared error across the three physical fields for 64 randomly sampled Reynolds numbers in $[2000, 3000]$. Across multiple training runs, the NewPINNs loss typically stabilizes between 10^{-4} and 10^{-3} after approximately 300 epochs, as illustrated in Figure 7. The oscillatory behavior observed in later epochs is likely associated with the network refining predictions in regions containing corner vortices.

Figure 8 compares predicted and reference velocity magnitude and pressure fields for several Reynolds numbers. The velocity fields exhibit good agreement in both structure and magnitude, with minor discrepancies in fine-scale vortex features. While the pressure fields appear visually different, this is largely due to their near-zero values throughout most of the domain. Importantly, the model correctly captures the localized negative pressure region in the upper-right corner, which is critical for the overall flow dynamics.

The L^2 errors for velocity magnitude and pressure as functions of the Reynolds number are shown in Figure 7. Errors generally remain below 10^{-2} across the parameter range. Larger errors near $Re = 2000$ and $Re = 3000$ are likely attributable to reduced training data density near the interval boundaries. Additionally, the grid-to-mesh conversion is only first-order accurate, which limits the achievable resolution. Given the mesh size $h_{\max} = 0.05$, a baseline interpolation error on the order of $h_{\max}^2 \approx 2.5 \times 10^{-3}$ is expected.

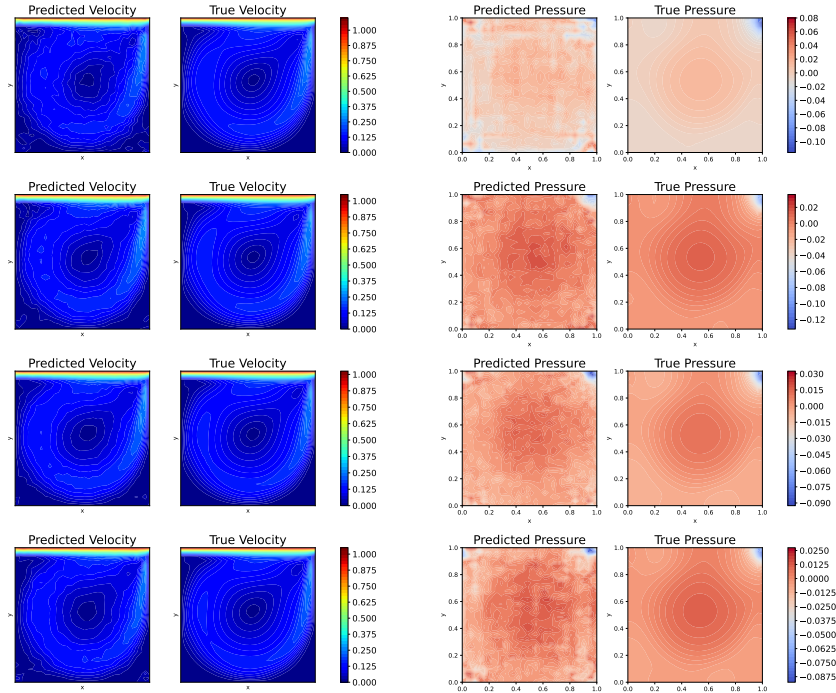


Figure 8: Predicted and true velocity magnitude fields (left) and pressure fields (right) for $Re = 2000, 2250, 2750$, and 3000 (top to bottom rows respectively)

A.3 1D Allen–Cahn Equation

Problem statement. The Allen–Cahn equation is a nonlinear parabolic partial differential equation that models diffusion–reaction processes such as alloy phase separation and crystal growth (Kim et al., 2020).

We consider the one-dimensional Allen–Cahn equation with periodic boundary conditions,

$$\frac{\partial u}{\partial t} - \alpha \frac{\partial^2 u}{\partial x^2} + 5u^3 - 5u = 0, \quad x \in [-1, 1], \quad t \in [0, 1], \quad (45)$$

where the diffusion coefficient satisfies $\alpha \in [10^{-4}, 10^{-3}]$. The initial and boundary conditions are given by

$$u(x, 0) = x^2 \cos(\pi x), \quad u(1, t) = u(-1, t), \quad u_x(1, t) = u_x(-1, t).$$

Numerical solver. We employ the Chebfun package in MATLAB as the coupled numerical solver (Driscoll et al., 2014). Chebfun represents functions using global polynomial or trigonometric interpolants and provides spectral accuracy for smooth problems. For periodic domains, Chebfun constructs trigonometric interpolants and effectively implements Fourier spectral methods (Trefethen et al., 2014; Trefethen, 2000, Chapter 11).

The spatial domain $[-1, 1]$ is discretized using $N = 101$ equally spaced points. For each fixed time t , the solution is approximated by a trigonometric interpolant

$$\mathcal{F}[u](x, t) = \sum_{k=-\infty}^{\infty} a_k(t) e^{ik\pi x}, \quad (46)$$

with Fourier coefficients

$$a_k(t) = \frac{1}{2} \int_{-1}^1 u(x, t) e^{-ik\pi x} dx. \quad (47)$$

In practice, the coefficients are approximated using an equally spaced grid

$$x_j = -1 + \frac{2j}{N}, \quad j = 0, \dots, N-1,$$

and the trapezoidal rule, yielding discrete coefficients

$$a_k(t) \approx c_k(t) = \frac{1}{N} \sum_{j=0}^{N-1} u(x_j, t) e^{-ik\pi x_j}. \quad (48)$$

The resulting interpolant

$$p_N(x, t) = \sum_{k=-N/2}^{N/2} \tilde{c}_k(t) e^{ik\pi x} \quad (49)$$

satisfies $p_N(x_j, t) = u(x_j, t)$ at the grid points. Under the assumption that $u(\cdot, t) \in C^\infty([-1, 1])$, the Fourier coefficients decay exponentially,

$$|c_k(t)| = \mathcal{O}(e^{-\beta|k|}), \quad \beta > 0,$$

leading to exponential convergence of the interpolant,

$$\|u(\cdot, t) - p_N(\cdot, t)\|_\infty = \mathcal{O}(b^N), \quad 0 < b < 1.$$

Spatial derivatives are computed spectrally. In particular, the second derivative is obtained in Fourier space via multiplication by $-k^2\pi^2$,

$$\frac{\partial^2 p_N}{\partial x^2}(x, t) = \sum_{k=-N/2}^{N/2-1} -k^2\pi^2 c_k(t) e^{ik\pi x}. \quad (50)$$

For time integration, we use the fourth-order exponential time-differencing Runge–Kutta scheme (ETDRK4), which is well suited for stiff nonlinear problems (Cox & Matthews, 2002). The semi-discrete system can be written as

$$\frac{du}{dt} = \alpha L u(t) + 5u(t) - 5u(t)^{\circ 3}, \quad u(0) = u_0, \quad (51)$$

where L denotes the spectral Laplacian and $u^{\circ 3}$ denotes element-wise cubing. The combination of spectral accuracy in space and ETDRK4 time integration yields highly accurate reference solutions.

Training NewPINNs. During training, the neural network takes as input the triplet (t, x, α) and outputs a prediction for $u(t, x; \alpha)$. The parameter range $\alpha \in [10^{-4}, 10^{-3}]$ is discretized with step size $\Delta\alpha = 10^{-4}$,

$$\alpha \in \{0.0001, 0.0002, \dots, 0.001\}.$$

The time interval is discretized using $\Delta t = 0.2$,

$$t \in \{0.0, 0.2, 0.4, 0.6, 0.8, 1.0\},$$

and the spatial domain is discretized with $\Delta x = 0.05$,

$$x \in \{-1.0, -0.95, \dots, 0.95, 1.0\}.$$

For each fixed (t^n, α) , the neural network is queried at all spatial locations to form an input array of shape $(N, 3)$,

$$\text{Input} = \begin{bmatrix} t^n & \alpha & x_1 \\ t^n & \alpha & x_2 \\ \vdots & \vdots & \vdots \\ t^n & \alpha & x_N \end{bmatrix},$$

which produces a vector-valued output

$$\hat{u}^n = [\hat{u}_1 \hat{u}_2 \dots \hat{u}_N].$$

This predicted state is treated as a virtual initial condition and advanced by the Chebfun solver to obtain u^{n+1} . Since the loss function compares solver outputs with network predictions at the next time step, the network must simultaneously predict \hat{u}^{n+1} . Accordingly, the input is augmented to include both time levels where the first N outputs correspond to \hat{u}^n and are passed to the solver, while the remaining N outputs correspond to \hat{u}^{n+1} and are compared against the solver result in the loss function.

We employ the MLP architecture introduced earlier, with a learning rate of 10^{-3} and batch size 32. All remaining hyperparameters follow the configuration described in Appendix A. For the inverse problem, the same configuration is used with an additional learning rate of 10^{-3} assigned to the parameter update. During training, the loss generally decreases over epochs, with occasional jumps corresponding to solver corrections of the neural network predictions. A final loss below 10^{-3} indicates that the network has successfully captured the solver-consistent dynamics.

Experimental results. Equation (45) exhibits smooth spatiotemporal behavior over the entire time interval. Figure 9 compares the neural network predictions with the Chebfun reference solutions at several time instances. The results demonstrate close agreement, indicating that the network accurately captures the underlying dynamics.

The minor numerical artifacts visible in the lower panels of Figure 9 arise from the intentionally coarse spatial discretization used during training. These artifacts can be mitigated by refining the spatial grid. The average L^2 error between the neural network prediction and the solver solution over the full space-time domain is 9.11×10^{-1} .

A.4 1D Kuramoto–Sivashinsky Equation

Problem statement. The Kuramoto–Sivashinsky (KS) equation is a nonlinear partial differential equation that exhibits deterministic chaos and spatiotemporal complexity. It arises in a variety of physical contexts, including flame-front instabilities, thin liquid film flows, and models of interfacial turbulence (Hoyle, 2006). We consider the one-dimensional KS equation with periodic boundary conditions,

$$\frac{\partial u}{\partial t} + u \frac{\partial u}{\partial x} + \alpha \frac{\partial^2 u}{\partial x^2} + \frac{\partial^4 u}{\partial x^4} = 0, \quad x \in [0, 100], \quad t \in [0, 20], \quad (52)$$

where the parameter satisfies $\alpha \in [1, 1.5]$. The initial condition is given by

$$u(x, 0) = \cos\left(\frac{x}{16}\right)\left(1 + \sin\left(\frac{x}{16}\right)\right),$$

and periodic boundary conditions are imposed on the spatial domain.

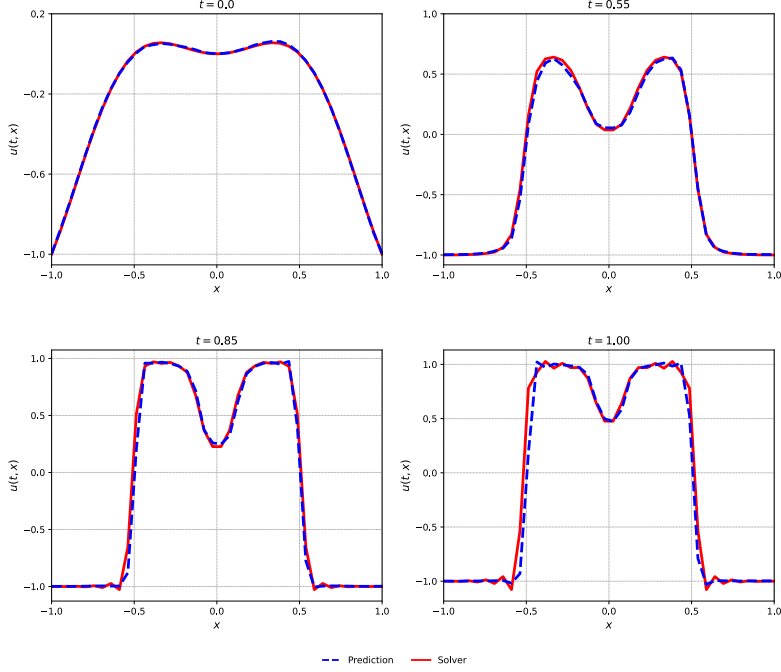


Figure 9: NewPINNs implementation on the Allen-Cahn equation for parameter $\alpha = 0.001$. Comparison between the neural network prediction and the solver solution at $t = 0.0, 0.55, 0.85, 1.00$.

Numerical solver. We solve (52) using the Chebfun package in MATLAB (Driscoll et al., 2014). As in the Allen–Cahn experiment, Chebfun represents periodic functions using trigonometric interpolants through its `trigfun` class, enabling Fourier spectral discretization in space (Trefethen et al., 2014, Chapter 11).

The spatial domain $[0, 100]$ is discretized with step size $\Delta x = 1$, corresponding to $N = 100$ equispaced grid points, and the solution is evolved over the time interval $[0, 20]$ using a time step $\Delta t = 0.02$. In Chebfun, the KS equation is split into linear and nonlinear components. The linear operator is defined as

$$\mathcal{L}[u] = \frac{\partial^2 u}{\partial x^2} + \frac{\partial^4 u}{\partial x^4}, \quad (53)$$

while the nonlinear term is given by

$$\mathcal{N}[u] = -u \frac{\partial u}{\partial x}. \quad (54)$$

Time integration is performed using the `spin` solver, which implements a fourth-order exponential time-differencing Runge–Kutta scheme (ETDRK4) (Cox & Matthews, 2002). All spatial derivatives are computed spectrally using fast Fourier transforms, providing high accuracy for smooth periodic solutions.

Training NewPINNs. As in Appendix A.3, the neural network inputs consist of the triplet (t, x, α) . The temporal, spatial, and parametric domains are discretized using step sizes $\Delta t = 1$, $\Delta x = 0.5$, and $\Delta \alpha = 0.05$, respectively, yielding the discrete sets

$$\begin{aligned} \alpha &\in \{1.00, 1.05, \dots, 1.50\}, \\ t &\in \{0.0, 1.0, \dots, 20.0\}, \\ x &\in \{0.0, 0.5, \dots, 100.0\}. \end{aligned}$$

Training batches are constructed from paired inputs (t^n, α, x) and (t^{n+1}, α, x) , following the same time-pairing strategy described in Appendix A.3. This allows the solver to advance the predicted state at time t^n and compare it with the network prediction at t^{n+1} during loss evaluation.

We employ a multilayer perceptron (MLP) architecture identical to that used in the Allen–Cahn experiment. The network is trained with a fixed learning rate of 10^{-3} and a batch size of 64, using randomly sampled inputs from the discretized domain. All remaining architectural and optimization hyperparameters follow the baseline configuration described in Appendix A.3. For the inverse problem, the same setup is used, with an additional learning rate of 10^{-3} applied to the parameter update step.

Experimental results. Equation (52) exhibits strongly chaotic behavior, characterized by sharp spatial gradients and rapid temporal evolution. Figure 10 compares neural network predictions with Chebfun reference solutions at representative time instances. The network accurately captures the large-scale structure and smooth regions of the solution. However, discrepancies are observed near sharp transitions, particularly at later times, as shown in the bottom-right panel of Figure 10.

These errors are consistent with the sensitivity of chaotic systems and the limited representational capacity of finite-width neural networks over long time horizons. Improved resolution of sharp features may be achievable through lower learning rates, increased model capacity, or extended training. The average L^2 error between the neural network prediction and the solver solution over the full space–time domain is 8.86×10^{-1} .

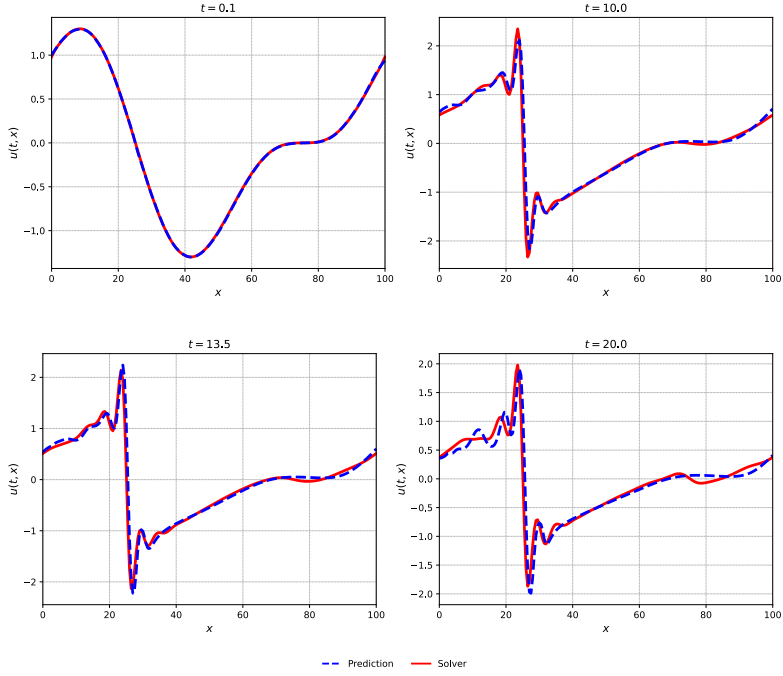


Figure 10: NewPINNs implementation on the Kuramoto–Sivashinsky equation for parameter $\alpha = 1$. Comparison between the neural network prediction and the solver solution at $t = 0.1, 10.0, 13.5, 20$.

B Ablation Studies

B.1 Forward Problem: Burgers' Equation

Problem statement. We conduct a systematic ablation study on a forward problem to assess the sensitivity of NewPINNs to architectural and optimization choices. As a canonical nonlinear test case, we consider the one-dimensional viscous Burgers' equation with Dirichlet boundary conditions,

$$\begin{aligned} \frac{\partial u}{\partial t} + u \frac{\partial u}{\partial x} &= \nu \frac{\partial^2 u}{\partial x^2}, & x \in [-1, 1], \quad t \in [0, 1], \\ u(x, 0) &= -\sin(\pi x), \quad u(t, -1) = u(t, 1) = 0. \end{aligned} \tag{55}$$

This equation provides a controlled setting for studying the interaction between nonlinear advection, diffusion, and solver–network coupling.

Numerical solver. We use a finite difference solver based on the forward-time central-space (FTCS) scheme (LeVeque, 2007c). The spatial and temporal domains are discretized as

$$\begin{aligned} x_i &= x_0 + i \Delta x, \quad i = 0, \dots, N, \\ t^n &= n \Delta t, \quad n = 0, 1, \dots, \\ u_i^n &\approx u(x_i, t^n). \end{aligned}$$

The temporal derivative, nonlinear convection term, and diffusion term are approximated by

$$\begin{aligned} \frac{\partial u}{\partial t} &\approx \frac{u_i^{n+1} - u_i^n}{\Delta t}, \quad u \frac{\partial u}{\partial x} \approx u_i^n \frac{u_{i+1}^n - u_{i-1}^n}{2\Delta x}, \\ \frac{\partial^2 u}{\partial x^2} &\approx \frac{u_{i+1}^n - 2u_i^n + u_{i-1}^n}{\Delta x^2}. \end{aligned}$$

This yields the update rule

$$u_i^{n+1} = u_i^n - \frac{\Delta t}{2\Delta x} u_i^n (u_{i+1}^n - u_{i-1}^n) + \frac{\nu \Delta t}{\Delta x^2} (u_{i+1}^n - 2u_i^n + u_{i-1}^n). \quad (56)$$

The FTCS scheme is conditionally stable, requiring the CFL constraints

$$\frac{u_{\max} \Delta t}{\Delta x} < 1, \quad \frac{\nu \Delta t}{\Delta x^2} < \frac{1}{2}$$

to hold throughout the simulation (LeVeque, 2007b). In our implementation, the solver accepts batched inputs for u^n and ν and advances each batch element in parallel. When multiple substeps are required, the update (56) is iterated N_s times within the solver.

Training NewPINNs. The neural network inputs consist of the triplet (t, x, ν) . The discretization parameters used during training are $\Delta t = 0.1$, $\Delta x = 5 \times 10^{-3}$, and $\Delta \nu = 0.01$, yielding

$$\begin{aligned} t &\in \{0.0, 0.1, \dots, 1.0\}, \\ \nu &\in \{0.01, 0.02, 0.03, 0.04, 0.05\}. \end{aligned}$$

A multilayer perceptron (MLP) with batch size 20 is used as the core architecture. The network depth and width are varied systematically to assess their impact on accuracy and training cost.

Experimental results. Figure 11 shows representative predictions for solver parameters $\Delta t = 5 \times 10^{-4}$ and $\Delta x = 5 \times 10^{-3}$. These results are obtained using a fully connected network with six hidden layers, 64 neurons per layer, tanh activations, a learning rate of 10^{-3} , and 40,000 training epochs.

Table 3 summarize the effect of varying the number of hidden layers and neurons per layer at fixed learning rate. Increasing network capacity generally improves accuracy but incurs higher computational cost. Among the tested configurations, a network with five hidden layers and 64 neurons per layer provides a favorable balance between accuracy and efficiency.

The impact of learning rate and training duration is examined in Table 4 for a fixed architecture with six hidden layers and 64 neurons per layer. A learning rate of 10^{-3} combined with 40,000 epochs yields the most accurate results among the tested settings, while further increases in training duration offer diminishing returns relative to computational cost.

Table 3: Relative L^2 error for Burgers' equation as a function of network depth and width. The learning rate is fixed to 10^{-3} and training is performed for 40,000 epochs.

Layers	Neurons per layer			
	16	32	64	128
1	3.06×10^{-1}	2.11×10^{-1}	2.34×10^{-1}	2.08×10^{-1}
3	7.75×10^{-2}	1.11×10^{-1}	7.17×10^{-2}	3.72×10^{-2}
5	7.61×10^{-2}	7.22×10^{-2}	6.91×10^{-2}	6.21×10^{-2}
7	1.64×10^{-1}	1.41×10^{-1}	4.36×10^{-2}	2.06×10^{-1}
10	1.87×10^{-1}	1.74×10^{-1}	4.06×10^{-2}	1.89×10^{-2}

Table 4: Relative L^2 error for Burgers' equation for varying learning rates and numbers of training epochs. The network architecture is fixed to 6 layers with 64 neurons per layer.

Learning rate	Training epochs			
	10k	20k	30k	40k
1×10^{-3}	1.21	1.18	5.54×10^{-2}	9.47×10^{-2}
5×10^{-4}	1.84	7.73×10^{-1}	6.17×10^{-1}	3.56×10^{-1}
1×10^{-4}	1.89	1.75	1.14	5.95×10^{-1}
1×10^{-5}	5.72	2.61	1.94	1.87

B.2 Inverse Problem: 1D Linear ODE

Problem statement. We next perform an ablation study on a simple inverse problem to examine the effect of network depth and data noise on parameter identification. The governing equation is a one-dimensional linear ODE,

$$\frac{dy}{dt} = -\alpha y + k, \quad t \in [0, 4], \quad (57)$$

where α is a decay rate and k is a source term. The analytical solution is

$$y(t) = \frac{k}{\alpha} + Ce^{-\alpha t}, \quad (58)$$

with constant C determined by the initial condition. The objective is to recover α and k from noisy observations of $y(t)$.

Numerical solver. We employ the forward Euler method (Ascher & Petzold, 1998), which yields the update

$$y^{n+1} = y^n(1 - \alpha\Delta t) + k\Delta t. \quad (59)$$

The solver operates in batch mode and is sensitive to the time step Δt . A convergence study with respect to Δt is performed using the analytical solution (58) as reference (Figure 12). Based on this study, $\Delta t = 0.01$ is selected for subsequent experiments.

Training NewPINNs. The neural network inputs consist of (t, α, k, y_0) . The discretization parameters are $\Delta t = 0.1$, $\Delta \alpha = 0.3$, $\Delta k = 0.5$, and $\Delta y_0 = 0.5$, yielding

$$\begin{aligned} t &\in \{0.0, 0.1, \dots, 4.0\}, \\ \alpha &\in \{0.1, 0.4, 0.7, 1.0\}, \\ k &\in \{-3.0, -2.5, \dots, 0.0\}, \\ y_0 &\in \{0.0, 0.5, \dots, 3.0\}. \end{aligned}$$

An MLP with 64 neurons per hidden layer is used, while the number of hidden layers is varied. A learning rate of 10^{-3} is applied to both the forward and inverse components.

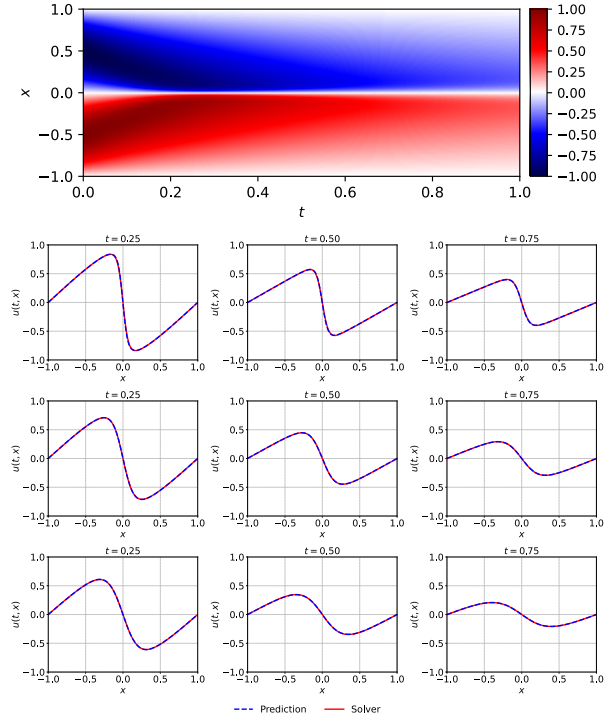


Figure 11: Burgers' equation for different kinematic viscosity ν (a) The network prediction of the solution over the entire time interval with $\nu = 0.01$. (b) Comparison between the network prediction and the solver at $t = 0.25, 0.50, 0.75$ for $\nu = 0.015$ (top), $\nu = 0.030$ (middle), and $\nu = 0.045$ (bottom).

Experimental results. We investigate the impact of network depth under increasing noise levels (1%–10%) added to the observed data. Figure 12 shows the reference and noisy datasets. The results summarized in Table 5 indicate that deeper networks yield more accurate parameter recovery, particularly in low-noise regimes. However, this improvement comes at increased computational cost, and higher noise levels consistently degrade identification accuracy.

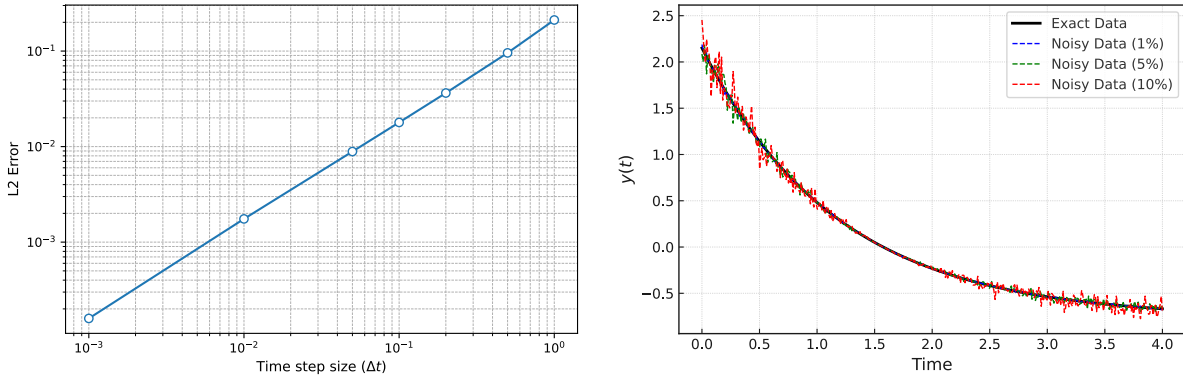


Figure 12: Results of the convergence study with respect to the time step Δt for the 1D linear ODE. Observed data with different levels of noise for the linear ODE.

Table 5: Percentage error in discovered decay rates α and source/sink terms k for various number of hidden layers under different noise levels. In all configurations, the neurons per hidden layer is set to 64. The learning rate is set to 1×10^{-3} for both the forward and inverse components, and training is performed over 40,000 epochs.

Noise Layers	% error in α				% error in k			
	0%	1%	5%	10%	0%	1%	5%	10%
1	3.23	5.65	10.87	15.21	2.82	2.93	6.70	10.36
3	1.54	1.36	3.12	5.55	1.31	2.03	2.73	7.46
5	0.75	1.04	1.10	2.33	0.65	0.61	1.91	2.53
7	0.66	0.51	1.49	2.39	0.72	0.43	2.19	3.12
10	0.07	0.12	1.27	3.24	0.38	0.09	1.72	3.42

C Additional Experiments

1D Linear ODE. We present additional experiments illustrating the application of NewPINNs to ordinary differential equations. We first revisit the one-dimensional linear ODE introduced in Section B, but omit the source/sink term k . The governing equation is therefore

$$\frac{dy}{dt} = -\alpha y, \quad t \in [0, 10], \quad (60)$$

which admits a closed-form analytical solution. The coupled solver is the forward Euler method.

The objective of this experiment is to train a neural network surrogate capable of predicting the temporal evolution of the solution over an extended time horizon. During training, the decay rate $\alpha \in [0.1, 1]$ and the initial condition $y_0 \in [1, 5]$ are sampled to promote generalization across parameter values.

We employ an MLP architecture with a learning rate of 10^{-3} and a batch size of 64. Figure 13 compares the neural network predictions with the analytical solution for multiple initial conditions. The average L^2 error across the tested cases is 2.90×10^{-3} , indicating accurate recovery of the underlying dynamics.

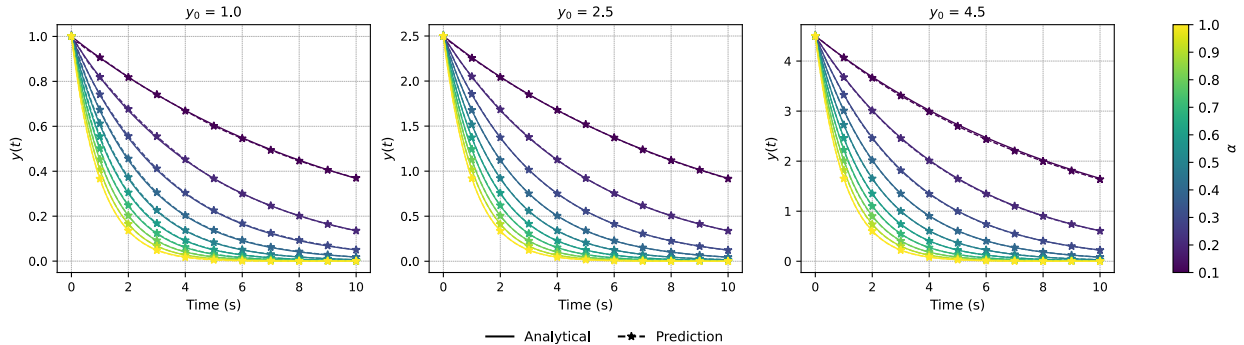


Figure 13: Comparison between the neural network prediction and the analytical solution for the 1D linear ODE across multiple initial conditions. The average L^2 error is 2.90×10^{-3} .

Nonlinear Lorenz system. We next apply NewPINNs to the Lorenz system, a classical nonlinear ODE system exhibiting deterministic chaos. The governing equations are

$$\frac{dx}{dt} = \sigma(y - x), \quad \frac{dy}{dt} = x(\rho - z) - y, \quad \frac{dz}{dt} = xy - \beta z, \quad (61)$$

with parameters $\sigma = 10$, $\rho = 28$, and $\beta = \frac{8}{3}$, which are standard benchmark values in chaos theory (Steven, 2015). The system is initialized at $(x_0, y_0, z_0) = (10, 10, 10)$ and evolved over the interval $t \in [0, 3]$.

On the solver side, we use the adaptive Runge–Kutta method implemented in SciPy’s `solve_ivp` routine (Virtanen et al., 2020). The adaptive time-stepping strategy automatically balances accuracy and efficiency, eliminating the need to prescribe a fixed time step.

The neural network surrogate is again an MLP trained with a learning rate of 10^{-3} and a batch size of 64. Figure 14 compares the neural network predictions with the numerical solver trajectories. While the model captures the overall structure of the solution over short time horizons, discrepancies grow as the system evolves deeper into the chaotic regime. The average L^2 error between the neural network prediction and the solver solution is 7.12×10^{-1} .

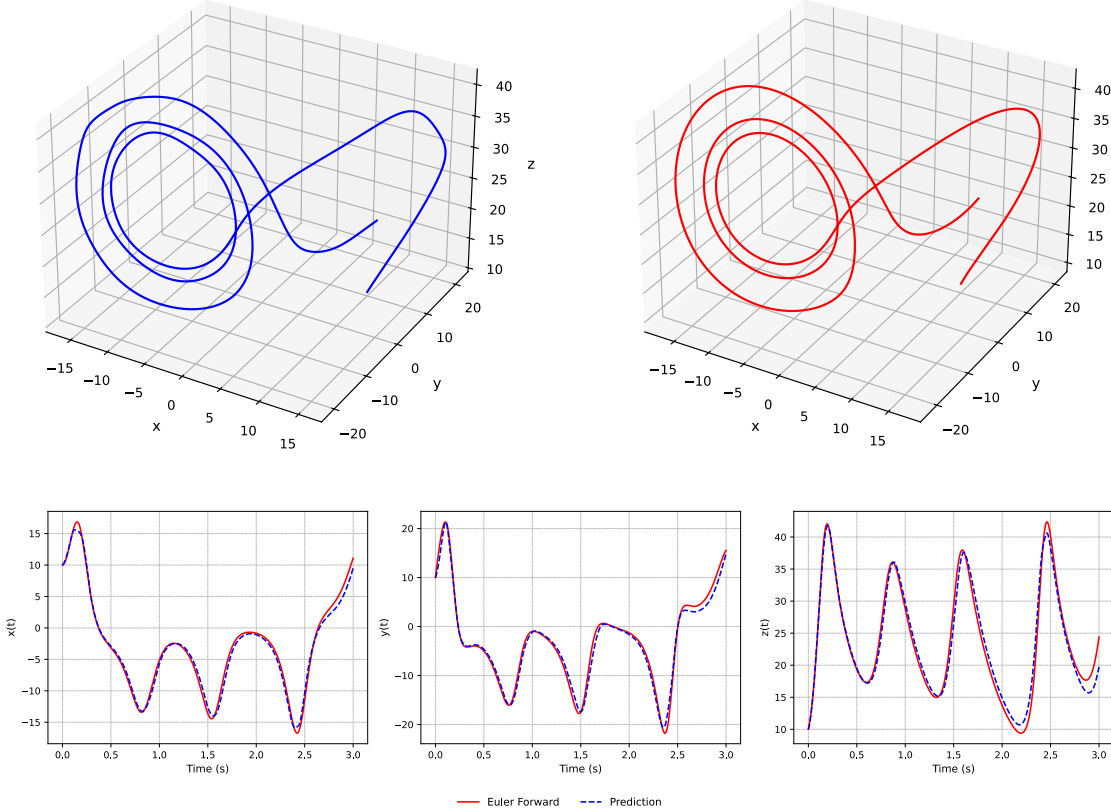


Figure 14: NewPINNs applied to the Lorenz system. Top: Phase-space trajectories over $t \in [0, 3]$. Bottom: Comparison between neural network predictions and solver solutions for $x(t)$, $y(t)$, and $z(t)$. The average L^2 error is 7.12×10^{-1} .